INSTITUTO POLITÉCNICO DE BRAGANÇA
Escola Superior de Tecnologia e Gestão

Influence of Web Holes on the Structural Design of Cellular Beams: Central Perforated Plate Buckling under Compression

César Hernández Leitão

Dissertation presented to the **School of Technology and Management, Polytechnic Institute of Bragança** in partial fulfillment of the requirements for the degree of Master in Mechanical Engineering.
(THIS VERSION DOES NOT CONTAIN ANY JUDGMENT OR APPRECIATION MADE BY THE MEMBERS OF THE JURY)

Supervisor: Prof. Dr. Luís Manuel Ribeiro Mesquita

october 2025

Abstract

Cellular steel beams gain their efficiency from circular, or other shapes, cutouts on the web panel, but these openings reduce compressive buckling capacity and trigger complex failure modes. This study quantifies the role of hole geometry in governing both elastic and plastic behaviors, developing design formulas that account for these effects. This process is made in three steps: An analytical stage, where using energy-based *Ritz* formulation, closed form for the critical buckling coefficient $k_{f,app.}$ of simply supported plates containing a circular cutout at the center, covering aspect ratios $1 \leq \beta \leq 4$ and cutout ratios $0.1 \leq d_f/b \leq 0.8$. This solution is only reliable for $d_f/b = 0.1$.

The numerical stage, where *Eigenvalue* buckling analysis and GMNIA are performed in *ANSYS*, that supported the validation of proposed equations, and reproduced mode switching phenomena (e.g., for odd β, the governing half-wave number m is always equal to β). Experimental stage, where compression tests on solid plates made from S235JR steel, with a thickness of $1.5mm$ confirmed the predictions within 0.82% for an aspect ratio of 1.1, and 0.96% for an aspect ratio of 1.5. These allowed the FEM calibration and the closed form model.

The parametric analysis, revealed an optimal design windows at $\beta = 2$ and $\beta = 4$, with a $d_f/b = 0.5$ ratio, delivering the highest buckling loads before plastic mechanisms arise. As for square plates, the hole centered, coincide with the maximum amplitude line, reducing its buckling capacity.

The resulting formulas predict the numerical solution with different accuracies. For fixed β values, the approximation is much better. The usage of approximated expression with double variables should be used only if really needed for other values different of β.

Contents

List of Figures

List of Tables

List of Symbols

$\mathbf{a}$	Plate length in the x-direction
$\mathbf{a_0}$	Opening length
$\mathbf{a_{eq}}$	Equivalent opening length for Vierendeel
$\mathbf{a_t}$	Effective top tee length
$\mathbf{A_{mn}}$	Ritz series coefficients (mode amplitudes)
$\mathbf{b}$	Plate width in the y-direction
β	Aspect ratio, $\beta = a/b$
χ	Twist curvature ($-\partial^2 w/\partial x \partial y$)
χ_{wp}	Reduction factor for web/web-post buckling
$\mathbf{D}$	Flexural rigidity of the plate
d_f	Hole diameter (via d_f/b cutout ratio)
e_o	Eccentricity of opening center from section centerline
$\mathbf{E}$	Young's modulus
ε_x	In-plane normal strain in x
ε_y	In-plane normal strain in y
f_y	Yield strength
γ	In-plane engineering shear strain
γ_{M0}	Partial factor for resistance (EC3)
γ_{M1}	Partial factor for instability (EC3)
$\mathbf{h_0}$	Opening height
$\mathbf{h_b}$	Bottom tee depth
$\mathbf{h_t}$	Top tee depth
$\mathbf{h_w}$	Web depth (slenderness checks)
$\mathbf{k}$	Buckling coefficient (depends on β)
k_f	Non-dimensional buckling coefficient for perforated plates
$k_{f,\text{app.}}$	Closed-form approximation to k_f
k_g	Global buckling coefficient (analytical development)
κ_x	Curvature about x ($-\partial^2 w/\partial x^2$)
κ_y	Curvature about y ($-\partial^2 w/\partial y^2$)
λ	Auxiliary parameter ($\pi^4 D/b^2$) in shear-buckling formulae
λ_w	Slenderness of web panel per EC3-1-13
λ_{wp}	Slenderness of web post
$\mathbf{m}$	Half-wave number in x (buckling mode index)
$\mathbf{m_x}$	Bending moment per unit length in x
$\mathbf{m_y}$	Bending moment per unit length in y

$\mathbf{m_{xy}}$ Twisting moment per unit length

$\mathbf{M_{0,Rd}}$ Bending resistance at opening section

$\mathbf{M_{Ed}}$ Design bending moment at opening

$\mathbf{M_{wp,Ed}}$ In-plane moment acting on web post

$\mathbf{n}$ Half-wave number in y (buckling mode index)

$\mathbf{n_x}$ Membrane force per unit length in x

$\mathbf{n_y}$ Membrane force per unit length in y

$\mathbf{n_{xy}}$ In-plane shear force per unit length

$\mathbf{N_x}$ Resultant compressive force per unit length in x

$\mathbf{N_y}$ Resultant compressive force per unit length in y

$\mathbf{N_{xy}}$ Resultant in-plane shear force per unit length

$\mathbf{N_{w,Ed}}$ Design compressive force in web at opening

$\mathbf{N_{w,Rd}}$ Design buckling resistance of compressed web

$\mathbf{N_{wp,Ed}}$ Effective horizontal force in web post

$\mathbf{N_{wp,Rd}}$ Web-post buckling resistance

$N_{\mathrm{cr},0}$ Critical buckling load for plate with central hole

ν Poisson's ratio

$\mathbf{q_x}$ Transverse shear force in x

$\mathbf{q_y}$ Transverse shear force in y

$\mathbf{R}$ Radius of the central hole

$\sigma_{b,w,\mathrm{Rd}}$ Design compressive stress of web (buckling)

$\mathbf{t_w}$ Web thickness

$\mathbf{t_{w,eff}}$ Effective web thickness at high shear

$\mathbf{u}$ In-plane displacement in x

$\mathbf{v}$ In-plane displacement in y

$\mathbf{V}$ Potential of external forces

$\mathbf{V_{0,pl,Rd}}$ Reduced shear resistance at perforation

$\mathbf{V_{b,Ed}}$ Shear at bottom tee

$\mathbf{V_{b,Rd}}$ Shear resistance of bottom tee

$\mathbf{V_{bw,Rd}}$ Shear buckling resistance of solid web

$\mathbf{V_{bw,o,Rd}}$ Shear buckling resistance of web with isolated opening

$\mathbf{V_{Ed}}$ Design shear at opening

$\mathbf{V_{pl,Rd}}$ Plastic shear resistance of the solid web

$\mathbf{V_{t,Ed}}$ Shear at top tee

$\mathbf{V_{t,Rd}}$ Shear resistance of top tee

$\mathbf{V_{w,Ed}}$ Design compressive force on web (slender webs)

$\mathbf{V_{w,o,Rd}}$ Design buckling resistance of the post (isolated opening)

$w(x,y)$	Transverse deflection of the mid-surface
Π	Total potential energy
U	Strain energy
U_b	Bending strain energy
U_m	Membrane strain energy

1 Introduction

Cellular steel beams are one type of thin walled structural element, where openings are introduced in the web for with multiple objectives and they are becoming fundamental components in lightweight construction. These elements are widely used in different sectors, such as, the aircraft industry, shipbuilding industry, in construction of industrial hangars, metallic structures, storage racking structures, etc. By allowing openings within the depth of the section, it is possible to reduce the dead weight of the structure, and easy consolidate with building services like piping, wiring, electrical-wiring, plumbing, allowing for compact ceiling and maximized floor-to-ceiling heights, without significantly compromise strength (Shanmugam & Dhanalakshmi, 2001). These properties, make them an optimal choice in scenarios where minimizing weight is critical. The unique structure of these beams allows to balance material usage with load bearing capacity, which supports the increasing demand for sustainable and efficient construction methods. When openings are induced within the depth of the beam, this arises several challenges, since it introduces complexities in the structural behavior, defying conventional design criteria, particularly related to stability under different loads.

Understanding, both elastic and plastic, buckling, is key to ensure reliability of these beams. Elastic buckling occurs when compressive forces reach a critical threshold value, leading to sudden lateral out-of-plane deformations. This phenomena, is governed by the *Euler's* critical load, which provides a theoretical background for predicting the initial stability of slender structures. In the work reported by (Timoshenko & Gere, 1989), this phenomena plays an important role in ensuring that beams maintain their structural integrity before any material yield.

Elastic stability by itself, in practice, is insufficient especially under dynamic or fluctuating loading conditions, and as discussed in (Bazant & Cedolin, 2010), the understanding by examining the post buckling behavior is essential, where plastic deformations allow for load redistribution after the initial instability occurs. Having these considerations in mind, the plastic design provides additional safety and resilience, allowing beams to withstand loads beyond their elastic limit without having immediate failure.

In context of cellular beams, web openings produce a redistribution of the plane stresses, changing the buckling and strength behavior. Independently of the applied stress on the plate, these openings position, size, location will impact the buckling resistance of these elements (Shanmugam & Dhanalakshmi, 2001). The openings introduce localized stress concentrations that can lead to premature buckling, posing as a point of weakness that will lower the critical buckling load. The openings, disrupt the continuity of stress field, which can accelerate localized buckling in those areas. It is with great importance, to have accurate and practical design equations to assess the critical buckling load of cellular beams, in order to guarantee the security of the whole structure as to optimize the quantity of steel used. Understanding how these parameters are linked, is crucial to define new safe design equations. Consequently, design criteria must account for these effects to avoid unexpected failures.

To help mitigate some of these vulnerabilities induced by the openings, the flange stiffness plays an important role. Both flanges (top and bottom), provide lateral and torsional restraint, avoiding excessive deflection and preventing the beam to twist under load. As (Timoshenko & Gere, 1989) highlight, this stiffness provides additional restraint to torsion, and can be valuable in beams with web holes. Increasing the flange stiffness, helps mitigating the reduced stability caused by the openings. Consequently, the importance of flanges stiffness and placement of the openings are dependent factors in determining the structural behavior of this type of beams. Based on these conditions, this research focus on develop/improve design formulations that account for these interactions under pure shear load, and establish design principles that optimize cellular beams performance without compromising stability. Through analytical analysis and Finite Element Analysis (FEA) validation, the purpose is to extend current stability models to consider real world conditions more accurately.

2 Literature Review

2.1 Elastic/Plastic Buckling

2.1.1 Theoretical Background of Elastic Buckling

Elastic buckling is a fundamental consideration in the stability analysis of cellular beams, especially those with slender, perforated webs. This happens when the web begins to lose stability under loading conditions, defined by buckling deformation without reaching the material's yield stress. The contribution of the web is critical in cellular structures, in terms of shear resistance, since the web carries the major portion of the shear buckling resistance (White & Barker, 2008), indicating the importance of the web's role in load bearing, especially in beams designed for high strength-to-weight ratios. As noted in (Ziemian, 2010), these critical stresses serves as an index for structural behavior, allowing to predict when the buckling might initiate. Since several configurations of perforation sizes, and geometrical properties of the web and flange, can be applied on cellular beams, it is imperative to develop practical equations, to assess the local stability of these sections, where the perforations decrease significantly the web's stability (Sweedan & El-Sawy, 2011). Post buckling behavior, helps redistributing the stress across the web after initial buckling, extending the load bearing capacity. This behavior becomes essential, especially where structures need to withstand dynamic loads. This post buckling strength contributes significantly to the overall load capacity, through tension field action. This tension field, according to (White & Barker, 2008), is a mechanism where diagonal stresses develop within the web post buckling, allowing additional loads to be sustained without failure. This is described by the transfer of loads along diagonal stress lines, which stabilizes the structure after buckling begins. If the web panel is thin enough, instead of yielding by shear, elastic buckling will take place, followed by post buckling strength development due to a diagonal tension field (Lee et al., 2012). The combination of elastic buckling analysis and post buckling behavior ensures that cellular beams perform accordingly under both static and dynamic loading conditions, making them the core consideration in early design stages.

2.1.2 Influence of web holes on buckling behavior

When web perforations are made, the buckling stability of structural elements is critically influenced by their size, shape, and spacing (Kang et al., 2021). Findings of (Kang et al., 2021), revealed that openings with circular or elongated shapes, and their spacing, affected directly the load carrying capacity, local buckling, and other collapse modes, such as, web post buckling and Vierendeel failure mode. Other study from (Zhu et al., 2022), related to perforated ship building steel plates, with different web cutout geometries, concluded that as the perforation size increased, the buckling resistance capacity decreased. In contrast, also stated by (Zhu et al., 2022), as the web thickness increases, the buckling resistance capacity also increases, proving the need for a balance between these two parameters (see figure 1). (Chen et al., 2018), also finds that welding-induced imperfections are important for plates with large holes, as the combined effects of reduced cross section area and residual stresses lead to a lower critical buckling load, especially for high slenderness ratios. Perforations along the web, which are the main a characteristic of these type of beams, introduce discontinuities that reduce the bearing load capacity, making this a crucial factor for structural stability and design (Sweedan & El-Sawy, 2011). The existence of web perforations, redistributes the longitudinal membrane stresses, combined with stress concentrations at the top and bottom parts of the perforation (Sweedan & El-Sawy, 2011).

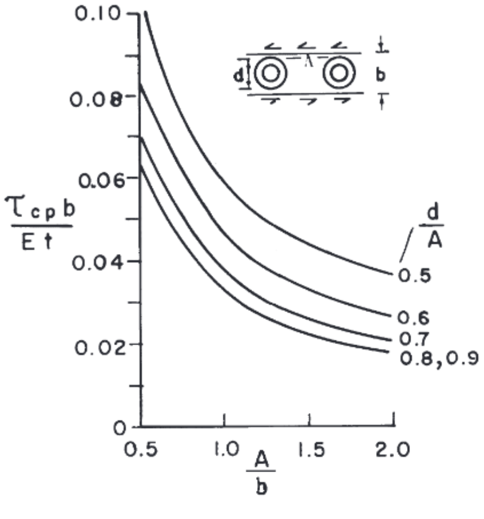

Figure 1: Critical shear stress for webs with openings (Ziemian, 2010).

Research on this topic about perforated I-girders, underscores the challenges introduced by web holes, which needs adjustments to traditional buckling design to prevent premature structural instability (Shanmugam & Dhanalakshmi, 2001). Detailed parameters for cross-sectional configurations and geometrical constraints, that impacts the stability of these elements with varying web characteristics, are the web aspect ratio (a/b), flange to web thickness ratio (t_f/t_w), flange width to web height (b_f/h_w), and direct stress ratio (ψ), as stated by (Lapira et al., 2023). While this study does not present directly buckling coefficients for perforated webs, it highlights the importance of tailored stability assessments when web discontinuities are present, as they reduce significantly the critical bearing load capacity. Elastic buckling of square plates with a central perforation, have been studied using numerical and experimental measurements, as done by (Kumai, 1952). This study compared approximate calculations of the critical load with model experiments to verify their accuracy, showing that the presence of openings significantly affects stability. Another study that used FEM to assess this parameter, was done by (Komur & Sonmez, 2008), analyzing the elastic buckling of a rectangular plate, where circular holes were placed in different locations of the web and examine their effect. It was found that in any position of the circular holes, even if not positioned in the critical location, the buckling load is always smaller than non perforated plates.

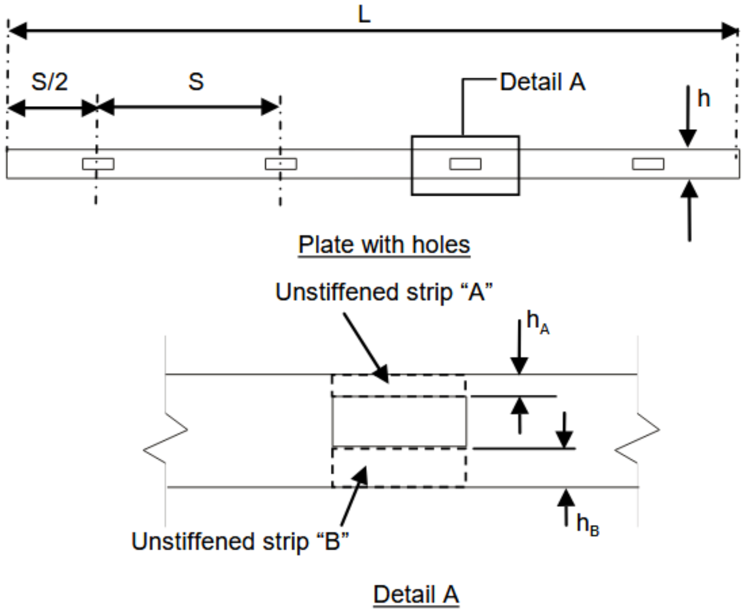

Figure 2: Schematic of unstiffened strips adjacent to a hole (Ziemian, 2010).

Figure 2, illustrates the unstiffened strips adjacent to holes, being relevant for understanding how different perforation configurations impact the stability. Cellular beam-column elements with perforated webs were also studied by (Sweedan & El-Sawy, 2011), where FEM was employed to analyze the effects of the interaction between the web and the flanges, and how different parameters are related, such as length, width, perforation diameter and spacing of the circular holes. Their findings agree with (Kumai, 1952) and (Ziemian, 2010), where the buckling load is decreasing with the presence of perforations.

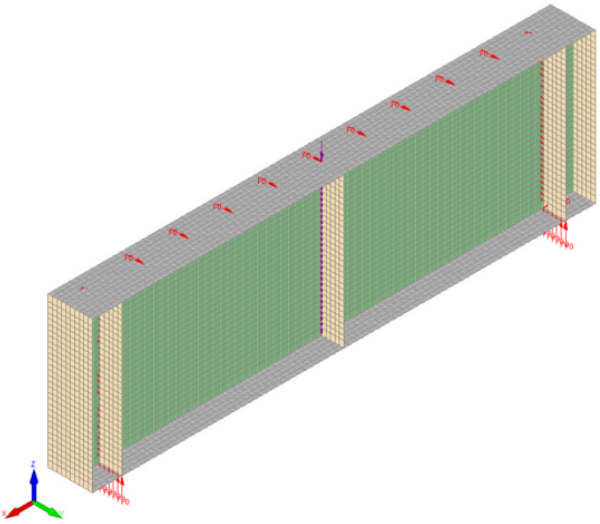

Figure 3: Finite element model used by (Reis et al., 2019), to obtain the ultimate shear stress .

In figure 3, numerical analysis were carried by (Reis et al., 2019), assessing the ultimate shear capacity using rigid and non rigid end posts. Eigenvalue buckling analysis were made using this model and determine the initial imperfections based on the first buckling mode, following the Eurocode 3 guide lines. This model simulates a simply-supported beam subjected to mid-span concentrated loading along the web depth (Reis et al., 2019). By employing rigid end posts, according to (Chen et al., 2018), there are significant gains in the ultimate shear carrying capacity in comparison with non-rigid end post configurations. In another study, (Tsavdaridis & D'Mello, 2011),made experimental, numerical and analytical procedures of perforated beams with closely spaced openings, evaluating the effect of the opening spacing to web opening depth ratio, and opening depth to web thickness ratio. The experimental tests carried by (Tsavdaridis & D'Mello, 2011), in seven steel specimens (two steel beams with circular openings, and five beams with non-standard web opening shapes), as seen in Figures 4 and 5. With respect to numerical models, they were validated through analytical/experimental procedures.

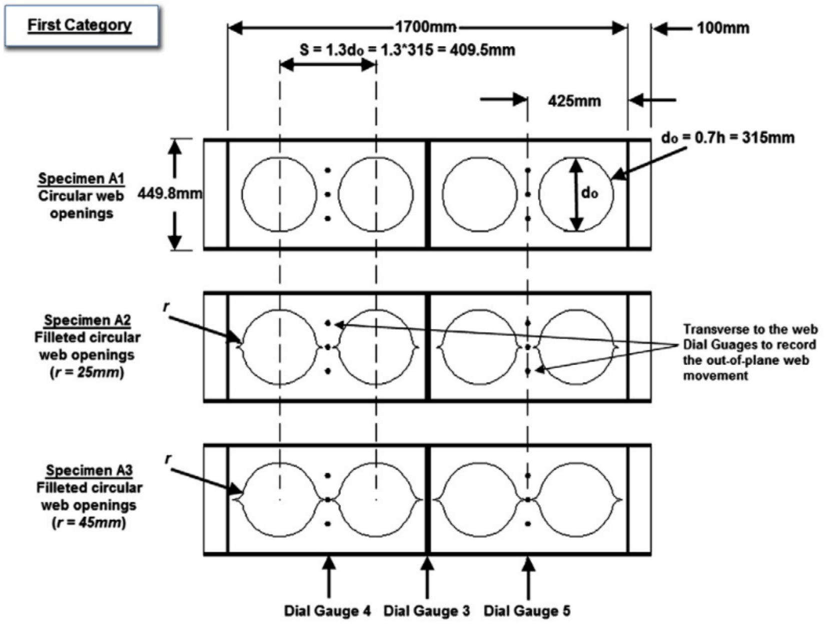

Figure 4: Specimen details and instrumentation (first category) (Tsavdaridis & D'Mello, 2011).

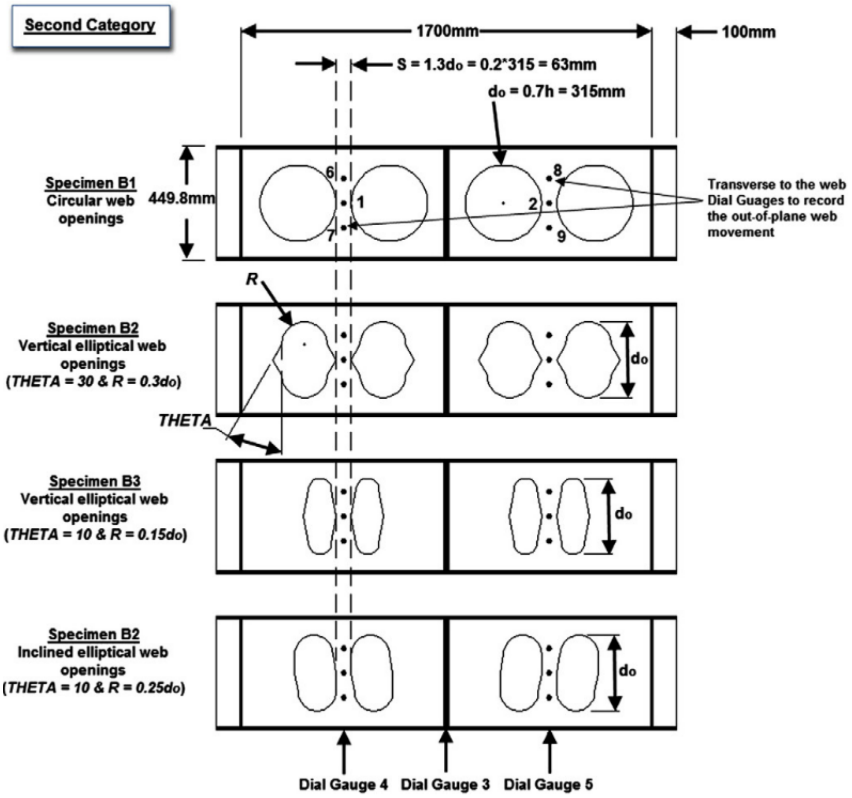

Figure 5: Specimen details and instrumentation (second category) (Tsavdaridis & D'Mello, 2011).

In the first category experimental tests, (Tsavdaridis & D'Mello, 2011), reported that at the notch point of the openings there was a very high stress concentrations. In the second category, (Tsavdaridis & D'Mello, 2011), refers to the comparison between specimens B1 and B2, where specimen B2 has almost 70% of the web opening area of specimen B1 and achieved 1.6 times the capacity of specimen B1. From this analysis, (Tsavdaridis & D'Mello, 2011), concludes that the critical opening length (c) (Figure 6), and not the opening area of the web, affects the beam's load carrying capacity.

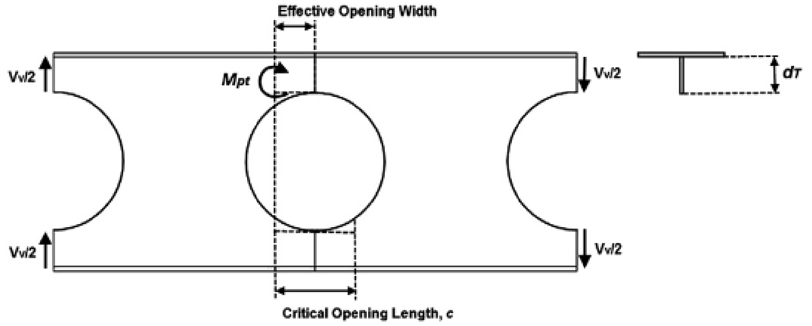

Figure 6: Geometric characterization of circular web openings in terms of effective width and critical length (Tsavdaridis & D'Mello, 2011).

2.1.3 Buckling modes in beams with web holes

In cellular beams, the principal buckling responses include local buckling, web-post buckling, distortional buckling, and the Vierendeel mechanism (L. Jia et al., 2024). Research by (L. Jia et al., 2024), shows that local buckling is a dominant failure mode in cellular beams, particularly in castellated beams with sinusoidal openings. Web post restraints and stiffeners can improve structural stability by enhancing the load capacity of the web, preventing premature failure (L. Jia et al., 2024). Also, (Shanmugam & Dhanalakshmi, 2001), local buckling tends to occur earlier when web openings are either large in size or closely spaced. Web-post buckling, which occurs due to deformation of the narrow web region between two openings, represents a critical instability in castellated beams. The extent of this instability is governed by the web-post width and the presence of stiffeners (L. G. Jia et al., 2020). Transverse stiffeners have been found to be effective in preventing post buckling of the web (L. G. Jia et al., 2020). Vierendeel mechanism is a failure mode that occurs in cellular beams due to shear stress redistribution around the opening, and it is characterized by localized bending and rotational deformations in the openings, which reduce the beam's ultimate capacity (Braga et al., 2021). (Wang et al., 2014), reported that the incorporation of fillet corner webs openings in castellated beams influences the Vierendeel failure mechanism, with results indicating improved load bearing capacity over beams with rectangular or hexagonal openings. According to (Wang et al., 2014), the primary characteristic of this failure mode is the development of plastic hinges at the end off the tee sections above and below the web perforation. Their findings also suggest that this mechanism can be attenuated by optimizing the spacing of the perforations and by increasing the web post thickness (Wang et al., 2014). By incorporating an M/V interaction equation in the design method was proposed to estimate the load bearing capacity of castellated beams under this mode of failure (Wang et al., 2014). In addition, distortional buckling has been identified as a mode of instability where both web and flange suffer coupled deformations (L. Jia et al., 2024). Such behavior is associated with beams simultaneously exhibit web distortional and web post buckling, decreasing the load bearing capacity (L. Jia et al., 2024).

2.1.4 Influence of hole position on the buckling behavior

(El-Sawy & Nazmy, 2001), have studied the influence of the hole size, shape, and position for uni axially loaded plates of different aspect ratios.

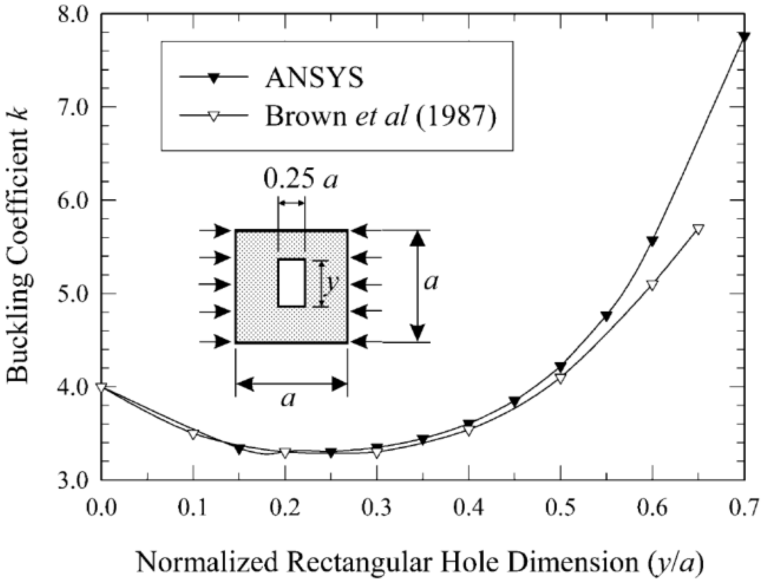

Figure 7: Comparison between buckling coefficients of finite element solution from (El-Sawy & Nazmy, 2001) and (Brown et al., 1987).

The solutions from Figure 7 are in clear agreement up to $y/a = 0.5$. Noticeably, as the y/a ratio is rising, the buckling factor k also increases. (El-Sawy & Nazmy, 2001), reported that the improvement in buckling resistance arises from the redistribution of the membrane stresses toward the laterally restrained edges of the plate. There is a trend, that can be easily identified for lower normalized hole ratios (d_f/b) that are below 0.5, for every aspect ratios analyzed. The buckling behavior of a rectangular plate ($\beta = 1, 2, 3, ..$), is approximately similar to a square plate, only when the hole is positioned in the outer half of the end panel ($x_e/b \leq 0.5$) with slightly higher values (Figure 8) (El-Sawy & Nazmy, 2001). Also, smaller holes dimensions ($d_f/b = 0.1$), has little effect on the buckling coefficient k, when higher values of x_e/b are used (El-Sawy & Nazmy, 2001).

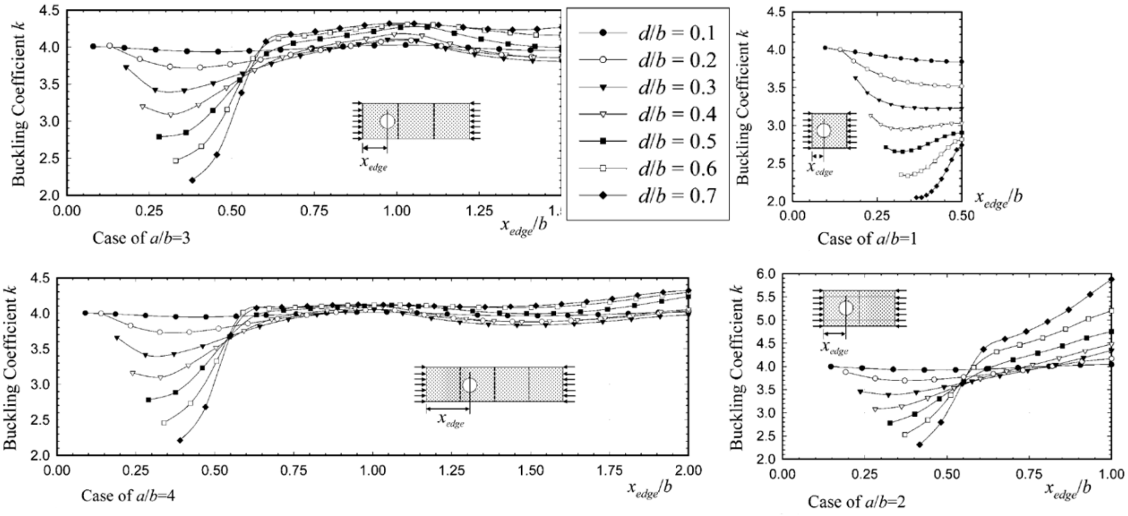

Figure 8: Parametric analysis of the normalized hole position (x_e/b) in the major axis of the plate, for different aspect ratios (El-Sawy & Nazmy, 2001).

According to (El-Sawy & Nazmy, 2001), for square and rectangular plates with holes positioned in the unfavorable range of $x_e/b = [0.25; 0.5]$ at higher d_f/b ratios (Figure 10). The hole ratio should be limited to 0.4 to achieve a buckling coefficient of at least $k \geq 3.0$. Outside this zone, the buckling factor shows limited variation with respect to hole size or location for rectangular plates, with the exception of cases where the plate has an aspect ratio of 2 and $x_e/b = 1$ (El-Sawy & Nazmy, 2001). In this particular case, when $d_f/b = 0.1$, the buckling coefficient has a value of 4.0 and it increases to a value of $k = 5.9$ when $d_f/b = 0.7$.

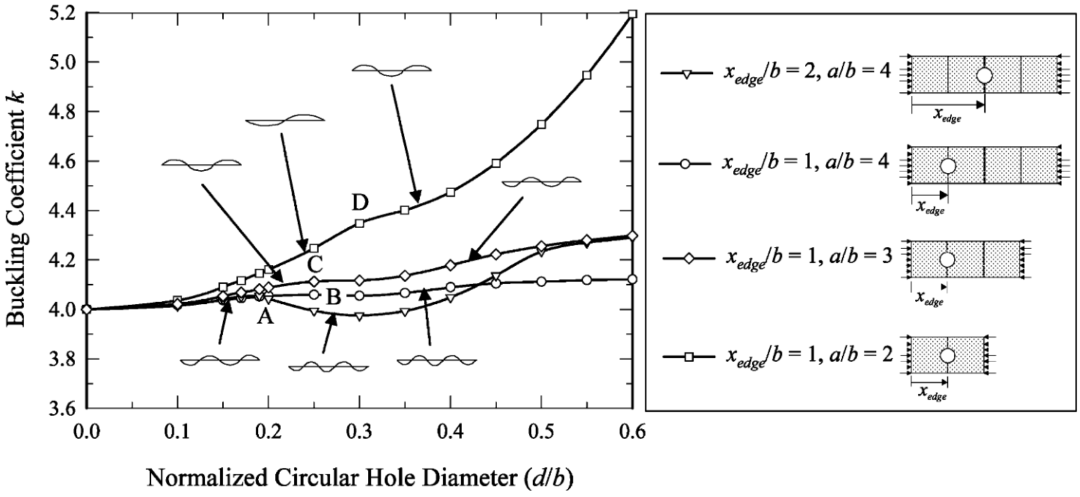

Figure 9: Buckling coefficient k for plates with a circular opening located at the intersection of a nodal line and the major axis (El-Sawy & Nazmy, 2001).

As shown in Figure 9, (El-Sawy & Nazmy, 2001) observed that the buckling coefficient k rises with increasing hole size, and discontinuities occur at points A, B, C, and, D.

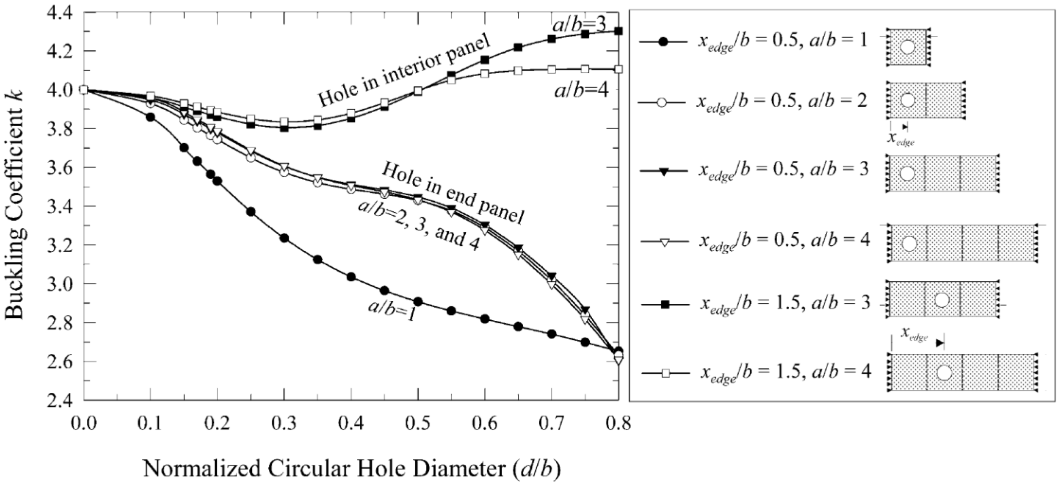

Figure 10: Buckling coefficient k for plates with a circular opening located on the major axis at a maximum amplitude cross line (El-Sawy & Nazmy, 2001).

(El-Sawy & Nazmy, 2001) observed that hole location exerts almost no influence on stability when the hole size is small ($d_f/b = 1$), although its impact increases with larger ratios (Figure 11). Their results also indicated that moving the hole farther from the nearest unloaded edge leads to improved plate stability, so it is recommended to keep this distance no more than $0.1b$, to have a $k \geq 3.4$ (El-Sawy & Nazmy, 2001).

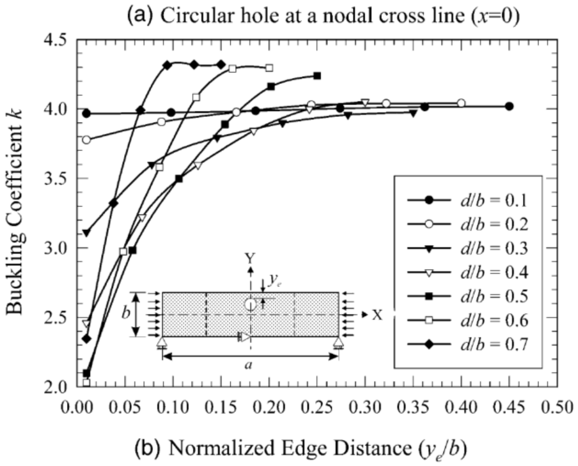
(a) Circular hole at a nodal cross line (x=0)

Circular hole at a cross line of maximum amplitude (x=b/2)

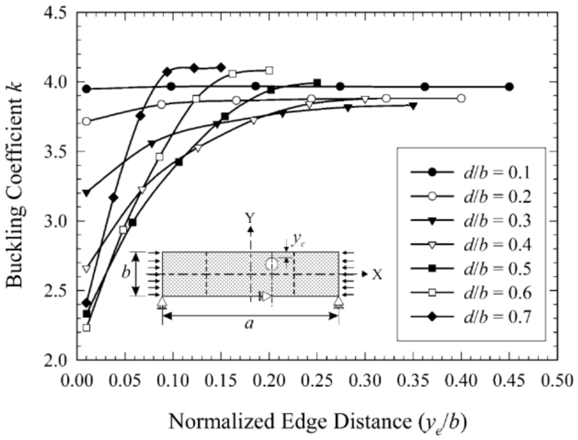

Figure 11: Buckling coefficient k of a rectangular plate with $\beta = 4$ containing a hole offset in the y-direction (El-Sawy & Nazmy, 2001).

2.2 Flange stiffness and its influence on buckling and plastic behavior

2.2.1 Role of flange stiffness in structural stability

Flange stiffness plays an important role in the buckling resistance and plastic behavior of cellular beams (Hingnekar & Vyavahare, 2023). This concept is defined as the resistance of the flange to deformation under applied loads and is governed by its thickness, width, and material properties (Hingnekar & Vyavahare, 2023). Stiff flanges improve the stability of the web panel by constraining deformations and buckling delay (Hingnekar & Vyavahare, 2023).Findings from (Hingnekar & Vyavahare, 2023) indicate that flange rigidity has a pronounced effect on the post buckling response of compact plates, though slender plates display different deformation patterns. Experimental work further demonstrated that flange stiffness improves the shear resistance of web panels and that increasing rigidity enhances both pre and post buckling strength, resulting in higher ultimate strength through plastic hinge development (Hingnekar & Vyavahare, 2023). As reported by (Mousa et al., 2021), flange to web interaction modifies both stress distributions and failure patterns in plate girders, with the effects being most evident under varying end stiffener conditions.

2.2.2 Interaction between flange stiffness and web holes

The interaction between these elements, is significantly affected by the presence of web perforations, which alter both buckling resistance and plastic behavior (Sweedan & El-Sawy, 2011). Flange stiffness has been shown to control elastic buckling loads and stress redistribution near the perforations, critically in cases of large perforation diameter to web height ratios (Sweedan & El-Sawy, 2011). Also, it governs post buckling behavior when acting combined with vertical stiffeners (Wang et al., 2019). (Wang et al., 2019), further noticed that using highly rigid flanges, leads to increased web post deformations, as the flange mechanism load (V_m) develops only after ultimate shear capacity (V_u) is attained. This implies that flange frame action contributes primarily once the web has yielded (Wang et al., 2019).

2.3 Plastic design of cellular beams

2.3.1 Plastic behavior in cellular beams

(Oribi et al., 2023), noted that when elastic limit is exceeded, beams show increasing plastic deformation, with web perforations affecting their structural performance and leading to failure modes, particularly concentrated in posts between closely spaced apertures. (França et al., 2022) demonstrated, as seen in Figure 13, that plastic behavior of cellular beams is governed by yield mechanisms and hinge formation around the openings. Figure 12 highlights the redistribution of stresses that induces plastic hinges at critical positions, generating local failures such as web post bucking and Vierendeel action (França et al., 2022).

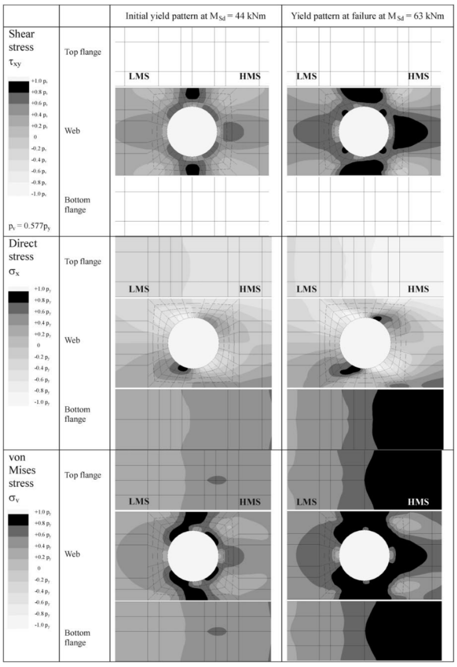

Figure 12: Stress redistribution at the perforated section in cellular beam tested by (Chung et al., 2001).

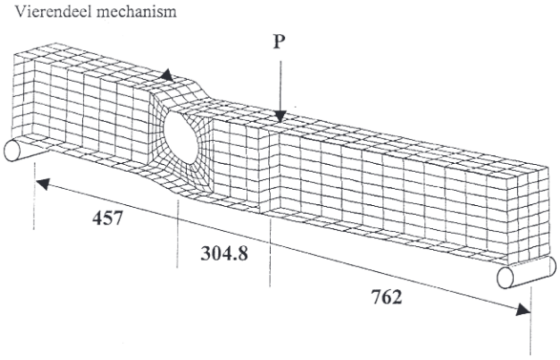

Figure 13: Finite element model with four plastic hinges (Chung et al., 2001).

2.3.2 Eurocode 3 Part1-13

Eurocode 3 Part 1-13 address the design of steel beams containing web perforations, incorporating the local and global bending, shear and axial forces effects (CEN/TC 250/SC 3, 2017). As described in the code, the equivalent rectangular method models the opening with an equivalent rectangle to estimate its shear resistance, which is derived from the local bending strength of the tee sections adjacent to the perforations (CEN/TC 250/SC 3, 2017). In Fig. 14, is possible to see the dimensions and shape of the equivalent rectangle openings, and in Table 1 the equivalent opening length and height.

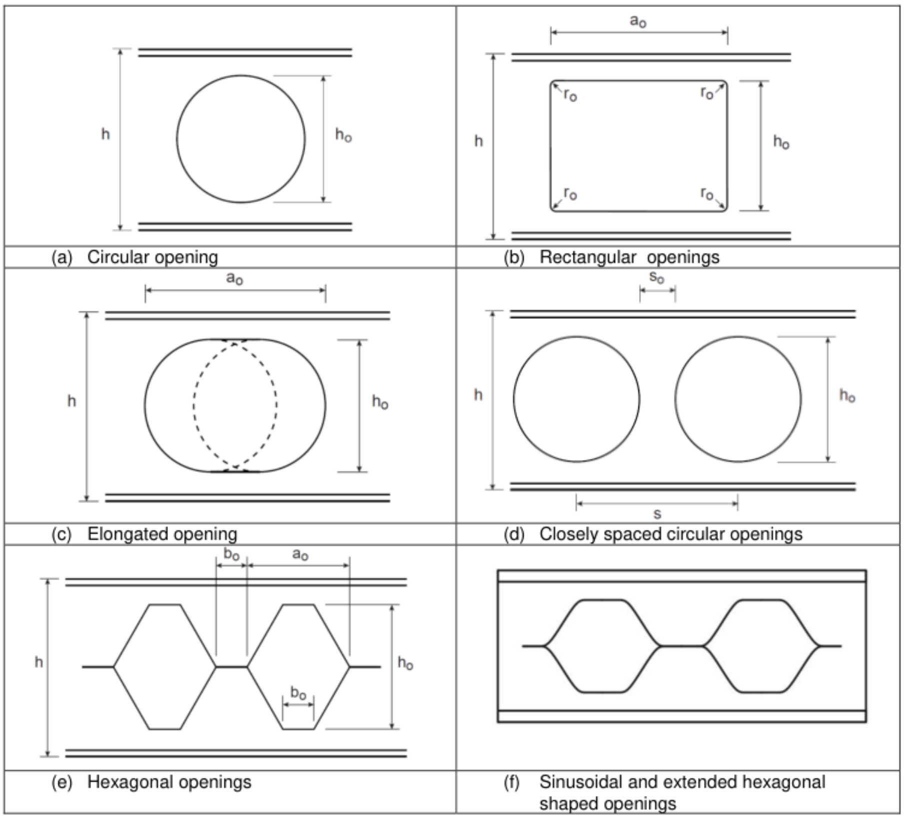

Figure 14: Different shapes of openings in steel beams (CEN/TC 250/SC 3, 2017).

Table 1: Equivalent rectangular opening dimensions for various opening shapes used in calculating Vierendeel bending resistance (CEN/TC 250/SC 3, 2017).

Shape of opening	Eq. opening length (a_{eq})	Eq. opening height (h_{eq})
Rectangular	a_0	h_0
Circular	$0.45h_0$	$0.9h_0$
Elongated circular	a_0-$0.55h_0$	$0.9h_0$
Hexagonal	b_0+$0.25h_0$	h_0
Sinusoidal	For $h_0 \leq 2b_s$: $a_{eq} = b_0 + 2b_s - 0.5h_0$	h_0
	For $h_0 > 2b_s$: $a_{eq} = b_0 + b_s$	h_0

There are limits imposed on maximum dimensions of openings without longitudinal stiffeners and the minimum depths of the Tees are present in Table 2.

Table 2: Maximum dimensions for different shapes of unstiffened openings (CEN/TC 250/SC 3, 2017).

Shape of opening	Maximum opening height	Maximum opening length	Minimum depth of top Tee
Circular	$0.8h$	-	h_t and $h_b \geq t_f + r + 10$ mm
Hexagonal	$0.75h$	$a_0 \leq 1.5h_0$	but $\geq t_f + 30$ mm
Rectangular	$0.75h$	$a_0 \leq 2.5h_0$	$h_t \geq a_0/12$
Elongated Circular	$0.8h$	$a_0 \leq 3h_0$	$h_t \geq a_t/12$
Sinusoidal	$0.8h$	$a_0 \leq 5h_0$	$h_t \geq a_t/12$

The value of a_t (effective length), should be calculated according the shape opening.
It is recommended that shear resistance at web perforations be verified using the plastic resistance of the tee sections (CEN/TC 250/SC 3, 2017). The design shear force V_{Ed}, taken at the centerline of the perforation, should therefore comply with:

$$V_{Ed}/V_{0,pl,Rd} \leq 1 \tag{1}$$

where,

$$V_{0,pl,Rd} = V_{pl,Rd} - \frac{h_0 t_w f}{\sqrt{3}\gamma_{m0}} \tag{2}$$

(CEN/TC 250/SC 3, 2005) (6.2.6), defines $V_{pl,Rd}$ as the plastic shear resistance of the solid web cross section. The standard further indicates that, for cases where $V_{Ed}/V_{0,pl,Rd} > 0.5$, the effective web thickness of the tee sections ($t_{w,eff}$) should be reduced to account for high vertical shear (CEN/TC 250/SC 3, 2005).

$$t_{w,eff} = t_w[1 - (2\frac{V_{Ed}}{V_{0,pl,Rd}} - 1)^2] \tag{3}$$

(CEN/TC 250/SC 3, 2017) specifies that the effective web thickness should be applied in computing the bending resistance of the tee sections to assess their shear resistance under Virendeel bending. Regarding web buckling, (CEN/TC 250/SC 3, 2017), when the slenderness of the web fulfills the condition given in (CEN/TC 250/SC 3, 2005) (6.2.6), Eq. 4, the resistance of a web next to an isolated opening needs to be verified.

$$\frac{h_w}{t_w} > 72\frac{\epsilon}{\eta} \tag{4}$$

(CEN/TC 250/SC 3, 2017) specifies that web buckling adjacent to an isolated opening, due to shear transfer from the tee sections into the web, must be verified through:

$$\frac{N_{w,Ed}}{N_{w,Rd}} \leq 1 \tag{5}$$

where $N_{w,Rd}$ is the design buckling resistance of the compressed web at the opening illustrated in Figure 15. The acting compressive force, $N_{w,Ed}$, is taken as the shear force on either top tee ($V_{t,Ed}$) or bottom tee ($V_{b,Ed}$) (CEN/TC 250/SC 3, 2017). The compressive force is expressed as (CEN/TC 250/SC 3, 2017):

$$\begin{aligned} N_{w,Ed} = V_{b,Ed} = V_{Ed}[\frac{V_{b,Rd}}{V_{b,Rd}+V_{t,Rd}}] \quad \text{for } V_{b,Ed} \geq V_{t,Ed} \\ N_{w,Ed} = V_{t,Ed} = V_{Ed}[\frac{V_{t,Rd}}{V_{b,Rd}+V_{t,Rd}}] \quad \text{for } V_{b,Ed} < V_{t,Ed} \end{aligned} \tag{6}$$

The resistance against web buckling is defined by (CEN/TC 250/SC 3, 2017):

$$N_{w,Rd} = b_w t_w \sigma_{b,w,Rd} \tag{7}$$

with the effective width of the compressed web, b_w, taken as $0.5h_0$ for unstiffened openings (CEN/TC 250/SC 3, 2017). The compressive stress of the compressed web, $\sigma_{b,w,Rd}$, is given as (CEN/TC 250/SC 3, 2017):

$$\sigma_{b,w,Rd} = \frac{\chi_{wp} f_y}{\gamma_{m1}} \tag{8}$$

where χ_{wp} is defined from the web slenderness ratios $\overline{\lambda_w}$, is given by (CEN/TC 250/SC 3, 2017):

$$\begin{aligned} \overline{\lambda_w} = \frac{2.4h_0}{t_w}\frac{1}{\lambda_1} \quad \text{for circular, hexagonal and elong. openings} \\ \overline{\lambda_w} = \frac{3.5h_0}{t_w}\frac{1}{\lambda_1} \quad \text{for rectangular openings} \end{aligned} \tag{9}$$

The non dimensional slenderness is defined as $\lambda_1 = \pi\sqrt{\frac{E}{f_y}} = 93.9\epsilon$, where E is the modulus of elasticity, and f_y is the yield strength. The design compressive stress for web buckling, $\sigma_{b,w,Rd}$, is evaluated using buckling curve ’a’ as specified in EN 1993-1-(CEN/TC 250/SC 3, 2017).

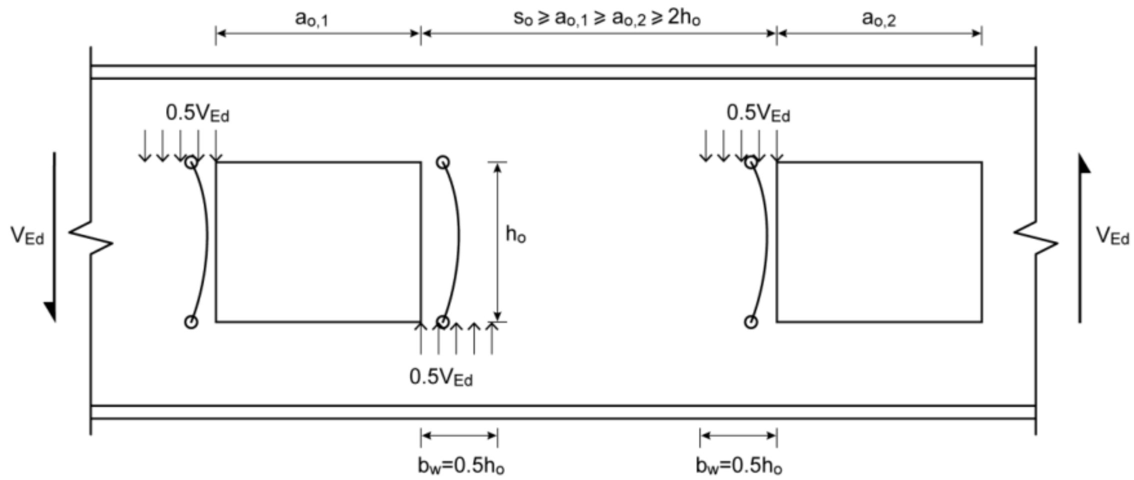

Figure 15: Model for web buckling next to widely spaced rectangle openings (CEN/TC 250/SC 3, 2017).

For slender webs, (CEN/TC 250/SC 3, 2017), verification of web buckling for an isolated opening is satisfied when:

$$\frac{V_{w,Ed}}{V_{w,o,Rd}} \leq 1.0 \tag{10}$$

The term $V_{w,Ed}$ refers to the design value of compressive force acting on the web, whereas $V_{w,o,Rd}$ denotes the design buckling resistance of the post. To account for the influence of an isolated opening, the shear resistance of a slender wen is evaluated using the following expression (CEN/TC 250/SC 3, 2017):

$$V_{bw,o,Rd} = 0.9V_{bw,Rd}(1 - \frac{\sqrt{h_o a_t}}{h_w}) \tag{11}$$

where the parameter $V_{bw,Rd}$ represents the shear buckling resistance of the solid web, as defined in Eq. 30 (CEN/TC 250/SC 3, 2017). According to the provisions outlined in (CEN/TC 250/SC 3, 2017), verification of web post buckling in the vicinity of a perforation is not required when:

$$\begin{aligned} h_o \leq 25t_w\epsilon \quad &\text{for circular, hexagonal and elong. openings} \\ h_o \leq 15t_w\epsilon \quad &\text{for rectangular openings} \end{aligned} \tag{12}$$

(CEN/TC 250/SC 3, 2017) provides specific guidance for the design of closely spaced perforations in webs. These openings are classified as closely spaced when the edge to edge distance between adjacent openings is less than $0.5s_0 = s_e$ as illustrated in Figure 16. Also, this is applied for a minimum web-post width of $s_0 \geq 0.1h_0$ for steel beams and with circular or hexagonal openings (CEN/TC 250/SC 3, 2017).

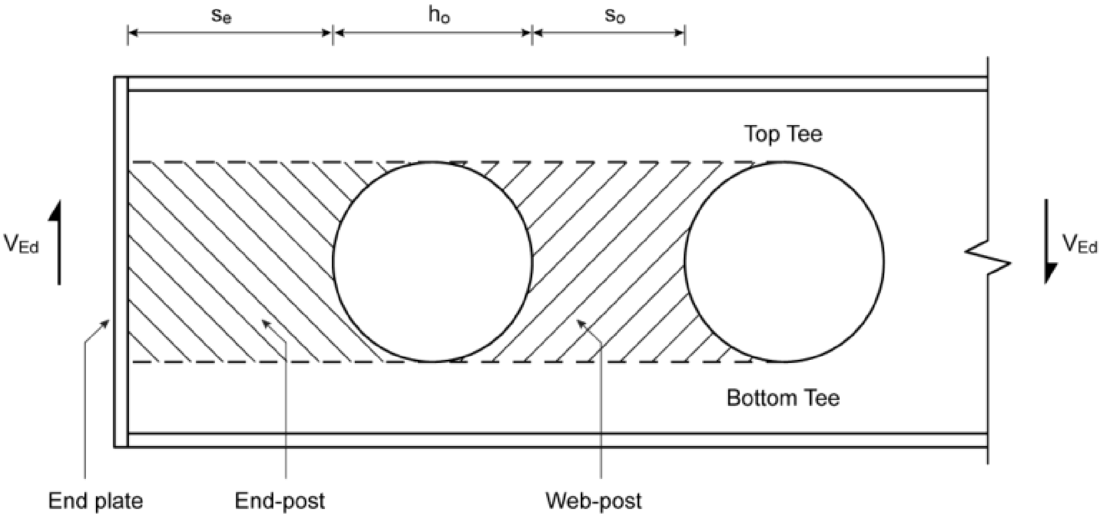

Figure 16: Definition of web post and end post for circular openings (CEN/TC 250/SC 3, 2017).

As illustrated in Fig. 17, the web post buckling model relies on the effective length of the compressed web post, which varies according to the geometry of the opening (CEN/TC 250/SC 3, 2017). Web post buckling is verified when (CEN/TC 250/SC 3, 2017):

$$\frac{N_{wp,Ed}}{N_{wp,Rd}} \leq 1 \tag{13}$$

where $N_{wp,Rd} = s_o t_{w,min} \sigma_{b,w,Rd}$ is the web post buckling resistance (CEN/TC 250/SC 3, 2017).

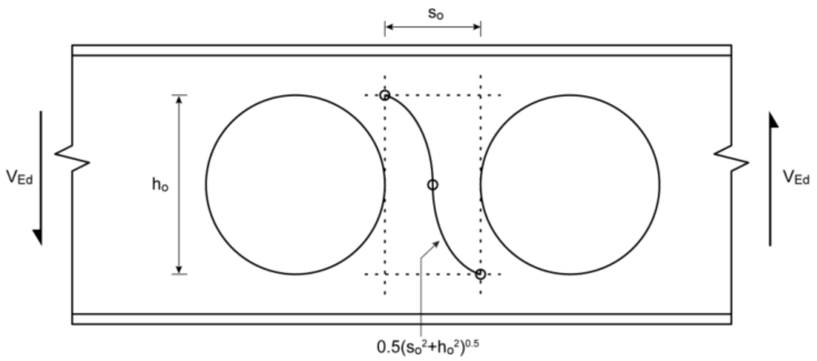

Figure 17: Buckling model for web posts between closely spaced circular openings (CEN/TC 250/SC 3, 2017).

For this verification, the compressive force acting on the web post, denoted as $N_{wp,Ed} = V_{wp,Ed}$ in Equation 13, is considered as the effective horizontal shear force within the web post (CEN/TC 250/SC 3, 2017). When the web posts are simultaneously subjected to an in-plane moment $M_{wp,Ed}$, the buckling analysis is performed by evaluating an effective horizontal force $N_{wp,Ed}$, which is defined as (CEN/TC 250/SC 3, 2017):

$$\begin{aligned} N_{wp,Ed} &= V_{wp,Ed} + 2M_{wp,Ed}/h_o \quad \text{top Tee} \\ N_{wp,Ed} &= V_{wp,Ed} - 2M_{wp,Ed}/h_o \quad \text{bottom Tee} \end{aligned} \tag{14}$$

where $M_{wp,Ed} = 0.5(V_{t,Ed} - V_{b,Ed})s + V_{wp,Ed}e_o$, with e_o measure as positive when the center of the opening lies above the section's centerline (CEN/TC 250/SC 3, 2017). The compressive stress acting on the web post is given by $\sigma_{b,wp,Rd} = \chi_{wp} f_y/\gamma_{M1}$, where the reduction factor χ_{wp} is determined from slenderness ratio $\overline{\lambda_{wp}}$, which varies depending on the shape of the opening (CEN/TC 250/SC 3, 2017):

$$\begin{aligned} \overline{\lambda_{wp}} &= \frac{1.75\sqrt{s_{o,eff}^2 + h_o^2}}{t_w}\frac{1}{\lambda_1} \leq \frac{2.4h_o}{t_w}\frac{1}{\lambda_1} \quad \text{Circular/Elongated circular openings} \\ \overline{\lambda_{wp}} &= \frac{1.75\sqrt{2s_{o,eff}^2 + h_o^2}}{t_w}\frac{1}{\lambda_1} \leq \frac{2.4h_o}{t_w}\frac{1}{\lambda_1} \quad \text{Hexagonal openings} \\ \overline{\lambda_{wp}} &= \frac{2.5\sqrt{s_{o,eff}^2 + h_o^2}}{t_w}\frac{1}{\lambda_1} \leq \frac{4.5h_o}{t_w}\frac{1}{\lambda_1} \quad \text{Rectangular openings} \end{aligned} \tag{15}$$

The value of $\sigma_{b,wp,Rd}$ cannot exceed the pure shear resistance of the web post (CEN/TC 250/SC 3, 2017):

$$\sigma_{b,wp,Rd} \leq \frac{f_y}{\sqrt{3}\gamma_{M0}} \tag{16}$$

To prevent shear failure and buckling of the end post adjacent to the connection, a verification based on force equilibrium is required (CEN/TC 250/SC 3, 2017). The slenderness of the end post is calculated using $\overline{\lambda_{wp}} = \frac{3.5h_o}{t_w}\frac{1}{\lambda_1}$, where h_o is the opening height (CEN/TC 250/SC 3, 2017). The compressive force considered for evaluating end post buckling corresponds to the horizontal shear force acting within the end post (CEN/TC 250/SC 3, 2017).

The bending resistance $M_{0,Rd}$ of a beam with openings, under the influence of shear at the opening location, is verified when the following condition is met (CEN/TC 250/SC 3, 2017):

$$M_{Ed}/M_{0,Rd} \leq 1 \tag{17}$$

where, $M_{0,Rd}$ is calculated using plastic bending resistance of the Tees for Class 1 or 2 sections, or the elastic bending resistance for Class 3 or 4 sections. To obtain the properties of the Tees in global bending, effective web thickness may be determined as above (CEN/TC 250/SC 3, 2017). The maximum length of the compressed Tee at a rectangular or elongated opening is determined by its buckling due to compression in global bending action (CEN/TC 250/SC 3, 2017). If $V_{Ed} \leq 0.25V_{0,pl,Rd}$, a simple verification of the maximum effective length of an unstiffened compressed Tee is given by:

$$a_t \leq 10h_t\epsilon\sqrt{M_{0,Rd}/M_{Ed}} \leq 12h_t \tag{18}$$

When $V_{Ed} > 0.25V_{0,pl,Rd}$, it should be accounted the additional eccentricity due to Vierendeel bending deflection across the opening, which can be taken as $a_0/50$ at the ultimate limit state (CEN/TC 250/SC 3, 2017).

The resistance to Vierendeel bending in tee sections is evaluated using an equivalent rectangular opening length (a_{eq}), as defined in Table 1 (CEN/TC 250/SC 3, 2017). At the location of the opening, the shear resistance must satisfy the Vierendeel bending criteria, expressed as (CEN/TC 250/SC 3, 2017):

$$V_{Ed}/V_{Vier,Rd} \leq 1 \tag{19}$$

The shear resistance to Vierendeel bending, denoted as $V_{Vier,Rd}$, is expressed as (CEN/TC 250/SC 3, 2017):

$$V_{Vier,Rd} = 2(M_{NV,b,Rd} + M_{NV,t,Rd})/a_{eff} \tag{20}$$

where $M_{NV,b,Rd}$, and $M_{NV,t,Rd}$, are the bending resistances of the bottom and top tee sections, respectively (CEN/TC 250/SC 3, 2017). These values are reduced to account for the effects of axial tension or compression and are calculated using the effective web thickness (CEN/TC 250/SC 3, 2017). The reduction in bending resistance due to axial force is determined using the following approximate expressions (CEN/TC 250/SC 3, 2017): Plastic resistance (Class 1 and 2 sections):

$$M_{NV,Rd} = M_{Pl,Rd}(1 - (N_{Ed}/N_{Pl,Rd})^2) \tag{21}$$

Elastic resistance (Class 3 and 4 sections):

$$M_{NV,Rd} = M_{El,Rd}(1 - N_{Ed}/N_{El,Rd}) \tag{22}$$

where N_{Ed} represents the design value of the axial compression or tension force induced by global bending, acting along the centerline of the opening (CEN/TC 250/SC 3, 2017). Eurocode 1993 Part1-13 provides an alternative approach for assessing Vierendeel bending, specifically applicable to hot rolled steel beams with equal circular openings (CEN/TC 250/SC 3, 2017). In this method, the overall bending and shear resistance of the beam must be verified at the center of the opening. The influence of Vierendeel moment is evaluated on a radial plane surrounding the opening, where ϕ represents the critical angle. This angle should be assessed in 5 increments, as illustrated in Figure 18 (CEN/TC 250/SC 3, 2017).

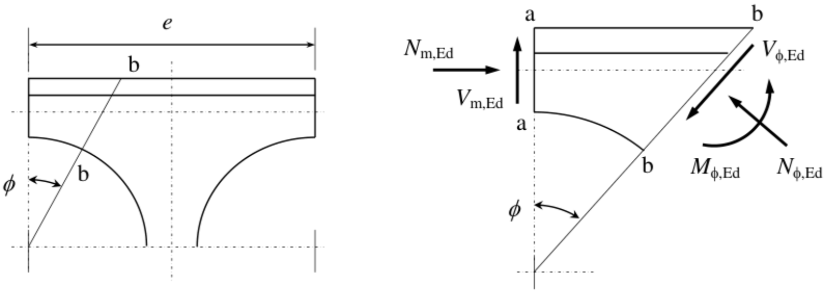

Figure 18: Distribution of internal forces and moments at the critical radial section around a circular opening (CEN/TC 250/SC 3, 2017).

When the critical angle for the effects of Vierendeel moments is found , the internal force $N_{\phi,Ed}$, and moment $M_{\phi,Ed}$, need to satisfy (CEN/TC 250/SC 3, 2017):

$$\frac{N_{\phi,Ed}}{N_{\phi,Rd}} + \frac{M_{\phi,Ed}}{M_{\phi,Rd}} \leq 1.0 \tag{23}$$

The skewed internal forces and moments observed at section b-b in Figure 18 are derived by evaluating the equilibrium of the segment between sections a-a and b-b, as outlines in (CEN/TC 250/SC 3, 2017). To account for the influence of the shear $V_{\phi,Ed}$, the design resistance values $N_{\phi,Rd}$ and $M_{\phi,Rd}$ must be determined (CEN/TC 250/SC 3, 2017). The shear force $V_{\phi,Ed}$ is calculated in accordance with Eurocode 1993 Part1-1 and must reflect the classification of the opening (CEN/TC 250/SC 3, 2017).

2.3.3 Eurocode 3 Part1-5

(European Committee for Standardization, 2006), provides the design requirements of stiffened and unstiffened solid, or with small cutouts, plated members that are subjected to in plane forces.

The interaction between transverse force, bending moment, and axial force is relevant when a concentrated transverse load is applied to the compression flange alongside bending and axial actions (European Committee for Standardization, 2006). In such cases, the member must satisfy the interaction criteria established by (European Committee for

Standardization, 2006):

$$\eta_1 = \frac{N_{Ed}\gamma_{M0}}{f_y A_{eff}} + \frac{(M_{Ed} + N_{Ed}e_N)\gamma_{M0}}{f_y W_{eff}} \tag{24}$$

where e_N is the shift in the position of the neutral axis, and W_{eff} is the effective elastic section modulus (European Committee for Standardization, 2006).

$$\eta_2 = \frac{F_{Ed}\gamma_{M1}}{f_{yw} L_{eff} t_w} \leq 1.0 \tag{25}$$

where F_{Ed} is the design transverse force, and L_{eff} is the effective length for resistance of transverse forces (European Committee for Standardization, 2006).

$$\eta_2 + 0.8\eta_1 \leq 1.4 \tag{26}$$

When the interaction involves shear force, bending moment, and axial force, and the parameter $\overline{\eta_3} \leq 0.5$, the design resistance to bending and axial load does not require reduction to account for the shear effects (European Committee for Standardization, 2006). However, if $\overline{\eta_3} > 0.5$, the combined influence of bending and shear in the web must satisfy the following interaction criterion (European Committee for Standardization, 2006):

$$\overline{\eta_1} + (1 - \frac{M_{f,Rd}}{M_{pl,Rd}})(2\overline{\eta_3} - 1)^2 \leq 1.0 \quad \text{for } \overline{\eta_1} \geq \frac{M_{f,Rd}}{M_{pl,Rd}} \tag{27}$$

where $M_{f,Rd}$ is the design plastic moment of resistance of the section consisting of the effective area of the flanges, $\overline{\eta_1} = \frac{M_{Ed}}{M_{pl,Rd}}$, and $\overline{\eta_3} = \frac{V_{Ed}}{V_{bw,Rd}}$ (European Committee for Standardization, 2006). Also, Eq. 24, and 29 needs to be satisfied.

Standard EN1993-1-5 does not provide shear buckling coefficients (k_τ) for unstiffened plates, since the equations provided depend directly of the spacing between transversal stiffeners. The equations of k_τ are (European Committee for Standardization, 2006):

$$\begin{aligned} k_\tau &= 5.34 + 4.00(h_w/a)^2 + k_{\tau sl} \quad \text{when } a/h_w \geq 1 \\ k_\tau &= 4.00 + 5.34(h_w/a)^2 + k_{\tau sl} \quad \text{when } a/h_w < 1 \end{aligned} \tag{28}$$

where $k_{\tau sl} = 9(\frac{h_w}{a})^2 \sqrt[4]{(\frac{I_{sl}}{t^3 h_w})^3}$, but not less than $\frac{2.1}{t}\sqrt[3]{\frac{I_{sl}}{h_w}}$,with a representing the distance between transverse stiffeners, I_{sl} denoting the second moment of area of the longitudinal stiffener about the z-z axis, and h_w being the web height (European Committee for Standardization, 2006). Also, (European Committee for Standardization, 2006), provides the values of η, which recommends a value of $\eta = 1.20$ for steel grades up to $460MPa$ of yield stress, and $\eta = 1.00$ for higher grades of steel.

The design resistance to shear for an unstiffened or stiffened web is defined by the (European Committee for Standardization, 2006):

$$V_{b,Rd} = V_{bw,Rd} + V_{bf,Rd} \leq \frac{\eta f_{yw} h_w t}{\sqrt{3}\gamma_{M1}} \tag{29}$$

where the web's contribution to shear resistance is expressed as (European Committee for Standardization, 2006):

$$V_{bw,Rd} = \chi_w f_{yw} h_w t / (\sqrt{3}\gamma_{M1}) \tag{30}$$

The flanges contribution are given by (European Committee for Standardization, 2006):

$$V_{bf,Rd} = \frac{b_f t_f^2 f_{yf}}{c\gamma_{M1}}(1 - (\frac{M_{Ed}}{M_{f_rd}})^2) \tag{31}$$

where $M_{f,Rd} = M_{f,k}/\gamma_{M0}$, denotes the moment of resistance of the cross section incorporating the effective area of the flanges only, and c is given as (European Committee for Standardization, 2006):

$$c = a(0.25 + \frac{1.6 b_f t_f^2 f_{yf}}{t h_w^2 f_{yw}}) \tag{32}$$

When axial forces are present N_{Ed}, the value of $M_{f,Rd}$ needs to be reduced by the factor (European Committee for Standardization, 2006):

$$(1 - \frac{N_{Ed}\gamma_{M0}}{(A_{f1} + A_{f2}) f_{yf}}) \tag{33}$$

where A_{f1} and A_{f2}, denote the areas of the top and bottom flanges respectively (European Committee for Standardization, 2006).

When transverse stiffeners are applied at supports only or with intermediate transverse stiffeners, the factor χ_w, for the contribution of the web to the shear buckling resistance can be obtained by Figure 19 (European Committee for Standardization, 2006).

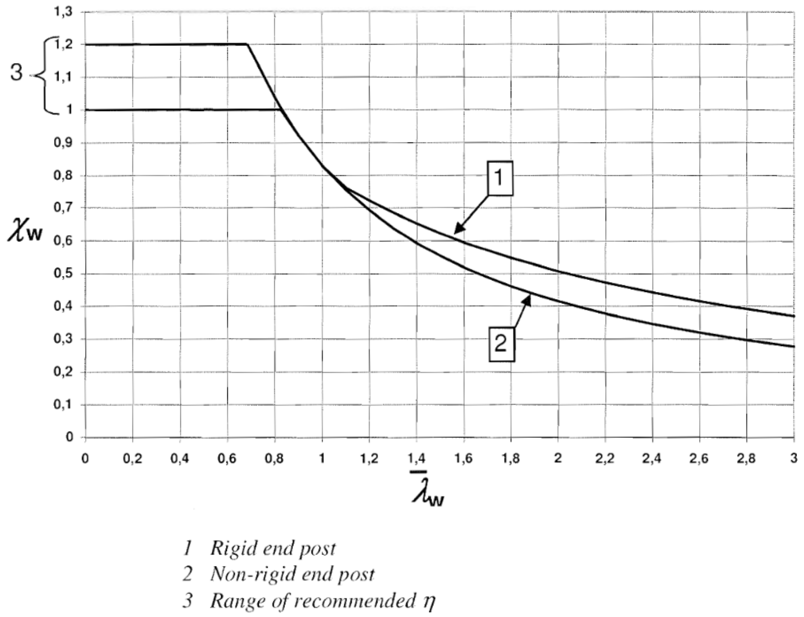

Figure 19: Shear buckling factor χ_w (European Committee for Standardization, 2006).

where $\overline{\lambda_w} = 0.76\sqrt{f_{yw}/\tau_{cr}}$ is the modified slenderness, $\tau_{cr} = k_\tau \sigma_E$ is the critical elastic shear buckling stress, and $\sigma_E = \pi^2 E t^2/(12(1-\nu^2)b^2)$ is the critical elastic buckling stress of the plate (European Committee for Standardization, 2006).

Regarding the shear resistance of plates, (European Committee for Standardization, 2006), states that plates with $h_w/t > (72/\eta)\epsilon$ for unstiffened configurations, must be checked for shear buckling resistance and equipped with transverse stiffeners at the supports, where $\epsilon = \sqrt{235/f_y}$ (European Committee for Standardization, 2006).

2.4 Validation through experimental and finite element method

This type of analysis is recognized as a proper numerical tool to assess the buckling and plastic behavior of structural components, and it is crucial to validate these models created in numerical environment with experimental procedures to validate their predictive capabilities. Literature findings reveal how finite element models are effectively validated against experimental procedures.

A numerical sensitivity analysis on the influence of initial imperfections and residual stresses (Figure 20) was carried by (Reis et al., 2016), and was validated against experimental models, revealing the accurate and reliable numerical predictions at normal and high temperature.

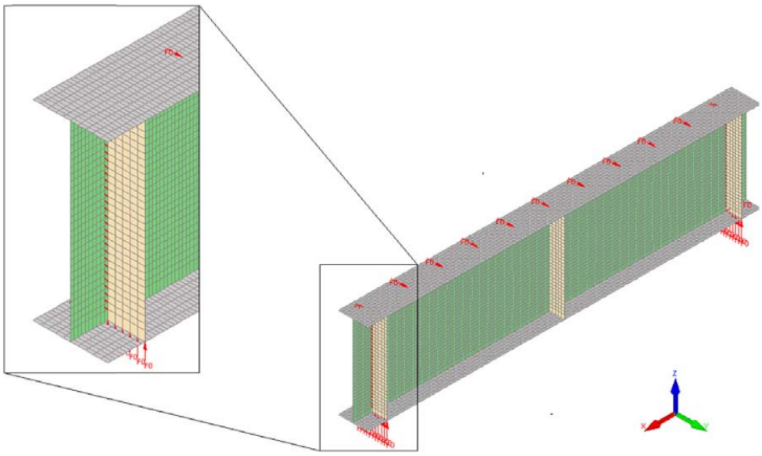

Figure 20: Numerical model from (Reis et al., 2016).

(Qiao & Shan, 2005) performed explicit buckling analyses on fiber reinforce plastic (FRP) composite beams using a variational formulation based on the Ritz method to derive the associated eigenvalue problem. Their analytical approach effectively captured local buckling behavior, including elastic flange-web interactions. Notably, the predicted buckling responses showed good agreement with results obtained from finite element analysis and experimental investigations, thereby validating the robustness of their theoretical model. (Braga et al., 2021), carried FEA to examine laterally braced castellated beams and evaluated their buckling and post buckling performance and were validated against experimental results available in literature (Figure 21).

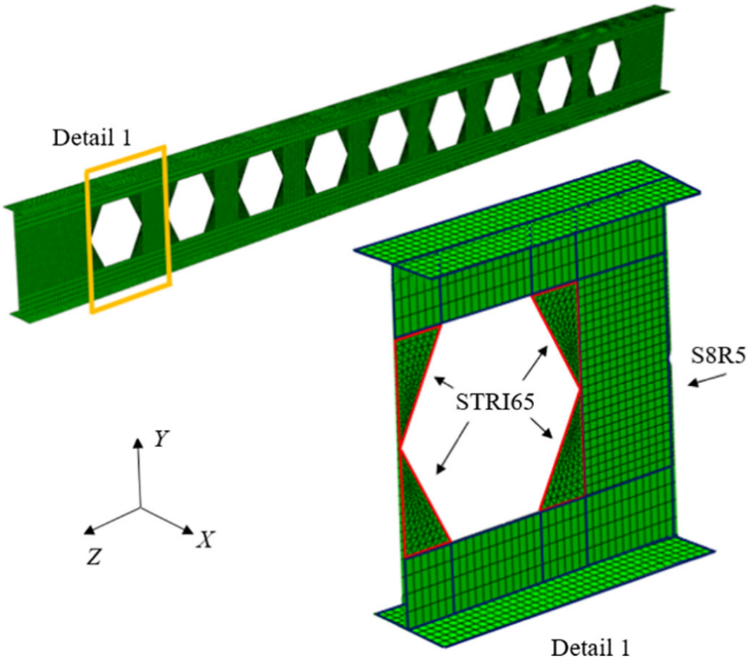

Figure 21: Numerical model from (Braga et al., 2021).

(Tsavdaridis & D'Mello, 2011) conducted finite element analyses incorporating nonlinear geometric and material properties to examine innovative web opening configurations in perforated steel beams. Their numerical simulations were rigorously validated through corresponding experimental tests, denoting strong correlation between simulated and observed structural behavior. (Wang et al., 2014) presented a practical M-V interaction equation for castellated beams and validated it using non linear FEA.
Based on these facts, FEA strongly supports the effectiveness of improved design formulas. The Ritz based model from (Qiao & Shan, 2005), was supported by numerical results, showing the importance and utility of closed-form analytical equations. The M-V interaction equation from (Wang et al., 2014), after being validated through FEA, the proposed design had much more sustain and credibility. In sum, FEA is an indispensable tool in validate and refine analytical developments, as seen in the studies above. They also confirm that, these analyses offer critical insights into structural response, that are key to develop more robust closed-form expressions.

2.5 Discussion and conclusions

The interaction between web perforations and flange stiffness, presents a critical parameter in structural stability. Within the elastic regime, web openings critically decreases the buckling resistance of cellular beams. As verified by (Ziemian, 2010), and (Sweedan

& El-Sawy, 2011), openings induce stress concentrations that disrupt the continuity of membrane stress, that can trigger local instabilities and lower shear buckling capacity. This phenomena, allied with closed spaced openings, can get much more complex with the introduction of web post buckling and Vierendeel mechanism failure modes (Tsavdaridis & D'Mello, 2011) (L. Jia et al., 2024).

To counter this weakness, flange stiffness plays an important role, where rigid flanges, as seen by (Wang et al., 2019), contribute to redistribute stresses after initial buckling. In highly perforated webs, the flange capacity to mitigate this effect is compromised, especially in the presence of post buckling and the initiation of plastic hinges. The studies from (Chung et al., 2001) and (França et al., 2022), focus attention on the transformation from local instability into global failure mechanisms, derived from the interaction from the stress fields around the web opening and flange stiffness. Eurocode 3 Part 1-13 proposes methodologies for isolated and closely spaced openings, but does not fully address the combined effect of flange stiffness and web openings under complex load schemes.

Taking in consideration all of these facts, this study fills the gaps found by proposing refined formulations, that will comprehend the effects of web openings and the stabilizing influence of flange stiffness under shear loads. Confirming these through analytical methodologies, experimental procedures, and FEA, this work establishes a more realistic approaches, reflecting better the real structural behavior.

This dissertation sums critical aspects from literature about the structural behavior of cellular steel beams, especially under elastic and plastic buckling conditions. To conclude, the development of improved design equations is with great importance, where it must account the effects of reduced web integrity with flange stiffness, and plastic failure modes. Overcoming these complexities, it is possible to benefit from the lightweight of cellular beams without compromising safety and performance.

3 Analytical development

(Szilard, 2004) explains that during the deformation of an elastic body, the work performed by external forces W_e is counteracted by the work of internal forces W_i. These internal forces are conservative in nature, meaning that upon removal of external loads, the structure reverts to its original state and the internal work is entirely recoverable (Szilard, 2004). Based on the principle of energy conservation, the total internal work must be equal in magnitude but opposite direction to the external work applied, and it is expressed as (Szilard, 2004):

$$W_e + W_i = 0 \tag{34}$$

According to (Szilard, 2004), potential energy represents the capacity of a force to perform work based on its positional configuration. In structural systems, the potential energy associated with internal forces is referred to as strain energy U, which corresponds to the negative of the work done bu these internal forces ($U = -W_i$) (Szilard, 2004). Similarly, the potential energy of external forces V, is defined as the negative of the work performed by these forces as they transition from their initial to final states while maintaining constant magnitude (Szilard, 2004). The total potential energy Π of a structural system is therefore expressed as the sum of its strain energy and the potential energy due to applied loads (Szilard, 2004):

$$\Pi = U + V \tag{35}$$

(Szilard, 2004) describes the stored strain energy in a deforming plate as the integral of the negative work performed by internal forces across the plate's middle surface. This strain energy comprises two distinct components: bending strain U_b and membrane strain energy U_m, and are respectively (Szilard, 2004):

$$U_b = \frac{1}{2}\int\int (m_x\kappa_x + m_y\kappa_y + 2m_{xy}\chi)dxdy \tag{36}$$

$$U_m = \frac{1}{2}\int\int (n_x\epsilon_x + n_y\epsilon_y + n_{xy}\gamma)dxdy \tag{37}$$

Here, m_x, m_y, m_{xy} represent the internal bending moments per unit length, and κ_x, κ_y, χ, are the corresponding curvature components, defined as (Szilard, 2004):

$$m_x = D(\kappa_x + \nu\kappa_y)m_y = -D(\kappa_y + \nu\kappa_x)m_{xy} = D(1-\nu)\chi \tag{38}$$

where $\kappa_x = -\frac{\partial^2 w}{\partial x^2}$, $\kappa_y = -\frac{\partial^2 w}{\partial y^2}$, and $\chi = -\frac{\partial^2 w}{\partial x \partial y}$ (Szilard, 2004).

Similarly, n_x, n_y, n_{xy} denote the membrane forces per unit length, and $\epsilon_x, \epsilon_y, \gamma$ are the corresponding in-plane strain components due to stretching (Szilard, 2004). Within the framework of small deflection plate theory, bending and membrane effects are decoupled and can be analyzed independently (Szilard, 2004). Although transverse shear forces q_x, q_y contribute to strain energy, their influence is negligible compared to bending effects and is therefore typically omitted from the energy formulation (Szilard, 2004). The work produced by external forces can be denoted as (Timoshenko & Gere, 1989):

$$V = -\frac{1}{2}\int\int(N_x(\frac{\partial w}{\partial x})^2 + N_y(\frac{\partial w}{\partial y})^2 + 2N_{xy}\frac{\partial w}{\partial x}\frac{\partial w}{\partial y})dxdy \tag{39}$$

(Szilard, 2004) highlights the application of variational methods as a powerful approach for solving complex boundary value problems in elasticity. These methods aim to indentify a set of admissible functions that accurately represent the deflection of an elastic body under equilibrium conditions (Szilard, 2004). When the equilibrium state is perturbed by introducing small variations in displacement $(u + \delta u, v + \delta v, w + \delta w)$, resulting in an increase in the stored strain energy (Szilard, 2004). The corresponding change in total potential energy $\delta\Pi$, is governed by the principle of stationary potential energy and is expressed as (Szilard, 2004):

$$\delta\Pi = \delta U + \delta V = \delta(U + V) = 0 \tag{40}$$

(Szilard, 2004) presents the Ritz method as a classical energy based technique for solving boundary value problems, grounded in the principle of minimum potential energy (see Eq. 40). The method asserts that, among all admissible displacement functions satisfying the boundary conditions, the configuration that minimizes the total potential energy corresponds to the actual deflection of the structure in stable equilibrium (Szilard, 2004). To approximate the deflected shape of the plate's middle surface, the displacement field $w(x, y)$ is expressed as a finite series (Szilard, 2004):

$$w(x, y) = c_1 f_1(x, y) + c_2 f_2(x, y) + ... + c_n f_n(x, y) = \sum_{i=1}^{n} c_i f_i(x, y) \tag{41}$$

where each function $f_i(x, y)$ for $i = 1, 2, 3, ..., n$, is continuous and individually satisfies the geometric boundary conditions, thereby enabling the representation of the plate's deflected surface (Szilard, 2004). The unknown coefficients c_n are determined by applying the principle of minimum potential energy. Minimizing the total potential energy expression (Eq. 35), leads to a system of n simultaneous algebraic equations (Szilard, 2004):

$$\frac{\partial\Pi}{\partial c_1} = 0, \frac{\partial\Pi}{\partial c_1} = 0, ..., \frac{\partial\Pi}{\partial c_n} = 0 \tag{42}$$

(Szilard, 2004) notes that, aside from the trivial solution corresponding to the unbuckled state of the plate, the system of equations derived from the Ritz method yields non-trivial solutions only when determinant of the coefficient matrix associated with the unknowns c_i vanishes. This condition signified the onset of buckling and transforms the problem into an eigenvalue-eigenvector formulation (Szilard, 2004). The resulting generic expression is expressed as (Szilard, 2004):

$$[A] - \lambda[I] = 0 \tag{43}$$

3.1 Buckling of simply supported solid plate under pure compression (N_x)

The deflection surface of the buckled plate can be written as (Timoshenko & Gere, 1989):

$$w(x, y) = \sum_{m=1}^{\infty}\sum_{n=1}^{\infty} A_{mn} cos(\frac{m\pi x}{a}) cos(\frac{n\pi y}{b}) \tag{44}$$

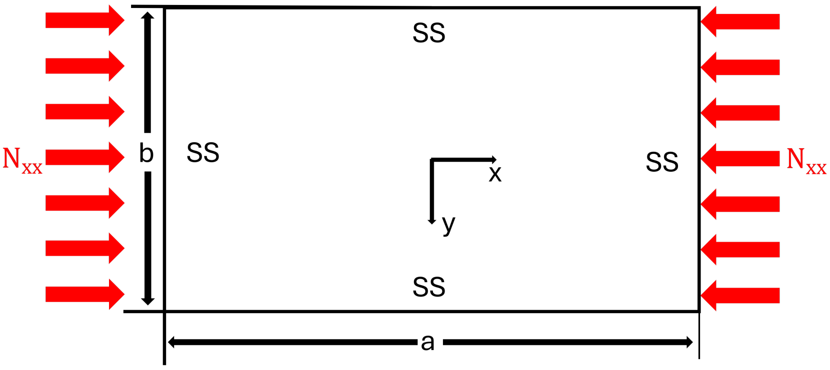

Figure 22: Simply supported solid plate under pure compression.

(Timoshenko & Gere, 1989) provides a formulation for the strain energy of bending in rectangular plates subjected to compressive forces. The bending strain energy U_b is expressed as (Timoshenko & Gere, 1989):

$$U_b = \frac{\pi^4 ab}{8} D \sum_{m=1}^{\infty}\sum_{n=1}^{\infty} A_{mn}^2 (\frac{m^2}{a^2} + \frac{n^2}{b^2})^2 \tag{45}$$

The work done by compressive forces during buckling of the plate (Timoshenko & Gere, 1989):

$$\frac{1}{2} N_x \int_0^a \int_0^b (\frac{dw}{dx})^2 dx dy = \frac{\pi^2 b}{8a} N_x \sum_{m=1}^{\infty}\sum_{n=1}^{\infty} m^2 A_{mn}^2 \tag{46}$$

(Timoshenko & Gere, 1989) demonstrates that the critical compressive force in plate buckling analysis can be determined by equating the strain energy due to bending with the work done by compressive forces. This energy balance condition is expressed mathematically as (Timoshenko & Gere, 1989):

$$\frac{\pi^4 ab}{8} D \sum_{m=1}^{\infty} \sum_{n=1}^{\infty} A_{mn}^2 (\frac{m^2}{a^2} + \frac{n^2}{b^2})^2 = \frac{\pi^2 b}{8a} N_x \sum_{m=1}^{\infty} \sum_{n=1}^{\infty} m^2 A_{mn}^2 \tag{47}$$

Solving Eq. 47 to N_x (Timoshenko & Gere, 1989):

$$N_x = \frac{\pi^2 a^2 D \sum_{m=1}^{\infty} \sum_{n=1}^{\infty} A_{mn}^2 (\frac{m^2}{a^2} + \frac{n^2}{b^2})^2}{\sum_{m=1}^{\infty} \sum_{n=1}^{\infty} m^2 A_{mn}^2} \tag{48}$$

According to (Timoshenko & Gere, 1989), the minimum critical compressive force N_x required to initiate buckling in a rectangular plate can be determined by considering the mode shape that yields the lowest energy configuration. This occurs when the plate buckles with a single half-wave in the direction perpendicular to the applied compressive force (i.e. $n = 1$), while multiple half-waves form along the direction of loading (Timoshenko & Gere, 1989). Under this condition, the critical compressive force is given by (Timoshenko & Gere, 1989):

$$N_{x,crit} = \frac{\pi^2 D}{b^2} (m + \frac{1}{m} \beta^2)^2 \tag{49}$$

where, $\beta = \frac{a}{b}$. By keeping the width b of the plate constant and increasing the length a, it is possible to see the variation of the parameter of Eq. 49 inside brackets, which only depends on geometrical parameters and the buckling mode m (Figure 23 and Table 3) (Timoshenko & Gere, 1989).

Table 3: Aspect ratio vs K factor interest values (simply supported edges).

β	K_{cr}	Buck. mode (m)	β	K_{cr}	Buck. mode (m)
0.4	8.410	1	1.0	4.000	1
0.5	6.250	1	1.2	4.134	1
0.6	5.138	1	1.4	4.470	1
0.7	4.531	1	1.6	4.420	2
0.8	4.420	1	1.8	4.045	2
0.9	4.045	1	2.0	4.000	2

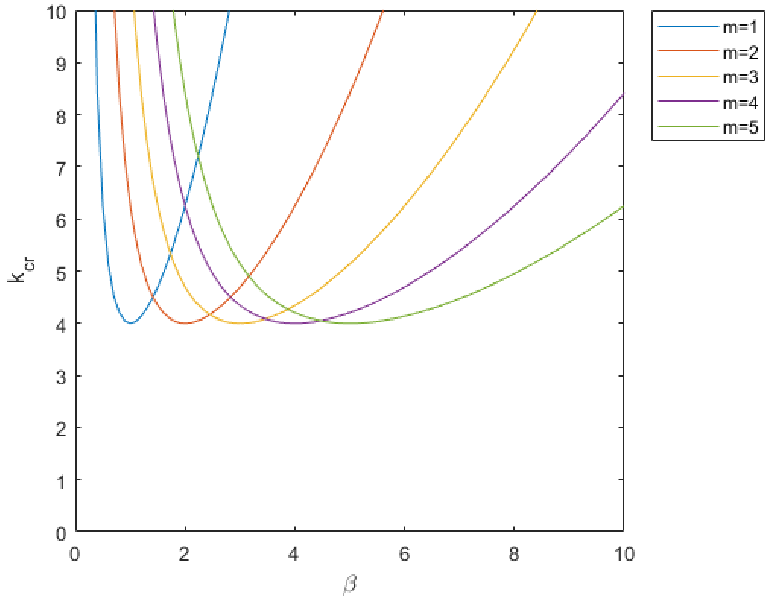

Figure 23: k values for solid plate under compression for different buckling modes ($m = 1, m = 2, ...$).

3.2 Buckling of clamped solid plate under pure compression (N_x)

The deflection surface of the buckled plate can be written as (Szilard, 2004):

$$w(x,y) = \sum_{m=1}^{\infty}\sum_{n=1}^{\infty} A_{mn}[1-(-1)^m cos(\frac{2m\pi x}{a})][1-(-1)^n cos(\frac{2n\pi y}{b})] \qquad (50)$$

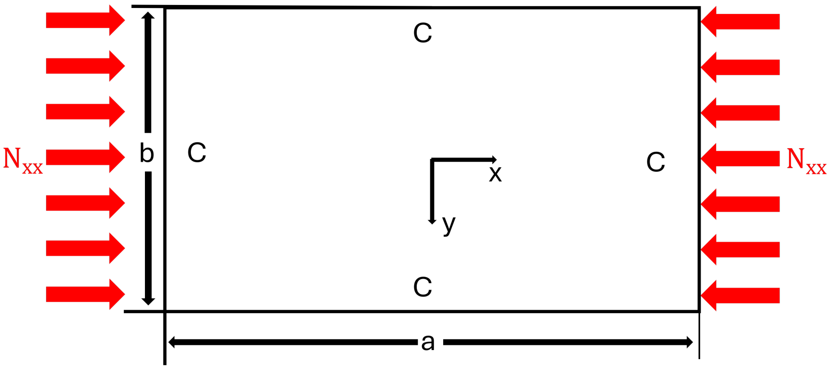

Figure 24: Clamped solid plate under pure compression.

The strain energy of bending becomes (Szilard, 2004):

$$U_b = D\pi^4 \sum_{m=1}^{\infty}\sum_{n=1}^{\infty} A_{mn}^2 \frac{3\beta^4 n^4 + 2\beta^2 m^2 n^2 + 3m^4}{a^2\beta} \tag{51}$$

The work done by compressive forces during buckling of the plate (Szilard, 2004):

$$V = -\frac{3}{2} N_x \sum_{m=1}^{\infty}\sum_{n=1}^{\infty} A_{mn}^2 \frac{bm^2\pi^2}{a} \tag{52}$$

To determine the critical value of the compressive forces, the strain bending energy must become equal to the work produced by the compressive forces, where (Szilard, 2004):

$$D\pi^4 \sum_{m=1}^{\infty}\sum_{n=1}^{\infty} A_{mn}^2 \frac{3\beta^4 n^4 + 2\beta^2 m^2 n^2 + 3m^4}{a^2\beta} = -\frac{3}{2} N_x \sum_{m=1}^{\infty}\sum_{n=1}^{\infty} A_{mn}^2 \frac{bm^2\pi^2}{a} \tag{53}$$

The total potential energy of the plate is (Szilard, 2004):

$$\Pi = (D\pi^4 \frac{3\beta^4 n^4 + 2\beta^2 m^2 n^2 + 3m^4}{a^2\beta} - \frac{3}{2} N_x \frac{bm^2\pi^2}{a}) A_{mn}^2 \tag{54}$$

Minimizing Eq. 54 ($\frac{\partial\Pi}{\partial A_{mn}} = 0$) and solving to N_x:

$$N_{x,crit} = \frac{\pi^2 D}{b^2}[\frac{4}{3m^2}(3\beta^2 n^4 + 2m^2 n^2 + \frac{3m^4}{\beta^2})] \tag{55}$$

Again, the smallest value of N_x, is obtained by taking $n = 1$ (Szilard, 2004). In the same way, keeping the width b constant and increasing the length a, the variation of the term inside the square brackets of Eq. 55, depends only on the geometric properties and the buckling modes (Figure 25 and Table 4) (Szilard, 2004).

Table 4: Aspect ratio vs K factor interest values (all edges clamped).

β	K_{cr}	Buck. mode (m)	β	K_{cr}	Buck. mode (m)
0.4	28.307	1	1.0	10.667	1
0.5	19.667	1	1.2	11.204	1
0.6	15.218	1	1.4	12.547	1
0.7	12.790	1	1.6	11.477	2
0.8	11.477	1	1.8	10.845	2
0.9	10.845	1	2.0	10.667	2

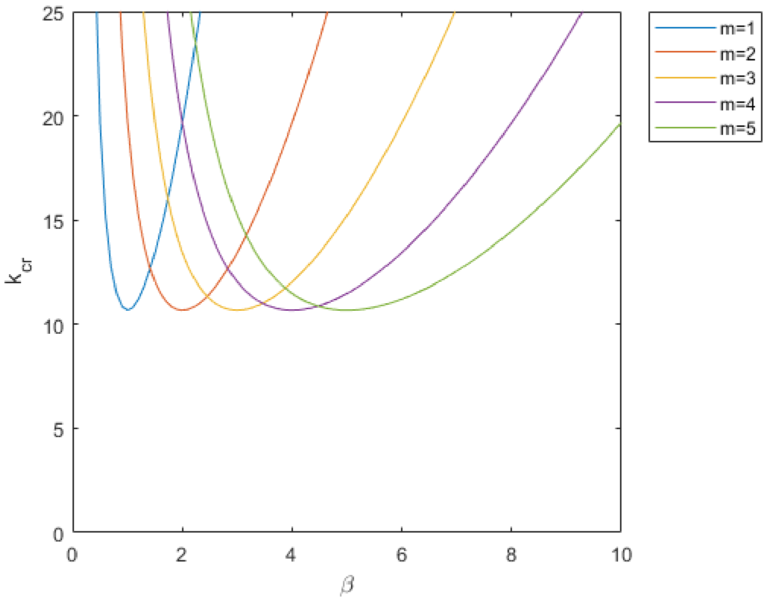

Figure 25: k values for solid plate under compression (all edges clamped) for different buckling modes ($m = 1, m = 2, m = 3, ...$).

3.3 Buckling of simply supported solid plate under pure shear (N_{xy})

By employing the same methodology as for the plate under compression, the strain energy bending Eq. 45 remains the same (Timoshenko & Gere, 1989). The work produced by the external forces during buckling of the plate (Timoshenko & Gere, 1989):

$$V = -N_{xy} \int_0^a \int_0^b \frac{dw}{dx} \frac{dw}{dy} dxdy \tag{56}$$

Introducing Eq. 44 into Eq. 56 (Timoshenko & Gere, 1989):

$$V = -4N_{xy} \sum_m \sum_n \sum_p \sum_q A_{mn} A_{pq} \frac{mnpq}{(m^2 - p^2)(q^2 - n^2)} \tag{57}$$

Here, the indices m, n, p, q are integers constrained such that $m \pm p$ and $n \pm q$ are odd, ensuring the appropriate symmetry and orthogonality conditions for mode interaction under shear loading (Timoshenko & Gere, 1989). The total potential energy (Π) of the plate is:

$$\Pi = \frac{\pi^4 ab}{8} D \sum_{m=1}^{\infty} \sum_{n=1}^{\infty} A_{mn}^2 (\frac{m^2}{a^2} + \frac{n^2}{b^2})^2 \\ + 4N_{xy} \sum_m \sum_n \sum_p \sum_q A_{mn} A_{pq} \frac{mnpq}{(m^2 - p^2)(q^2 - n^2)} \tag{58}$$

To determine the critical shear load N_{xy}, (Timoshenko & Gere, 1989) proposed minimizing the total potential energy of the plate by setting its first variation to zero, i. e., $\frac{d\Pi}{dA_{mn}} = 0$. This condition leads to a system of homogeneous linear equations in the mode shape coefficients A_{mn}, which can be categorized into two distinct groups based on the parity of the sum $m + n$: one group where $m + n$ is odd, and another where $m + n$ is even (Timoshenko & Gere, 1989). For plates with a short aspect ratio, $\beta < 2$, the second group ()$m + n$ is even) yields lowest critical shear load (Timoshenko & Gere, 1989). In contrast, for longer plates, both groups must be considered to accurately determine the minimum value of N_{xy} (Timoshenko & Gere, 1989).

By expressing the system in matrix form $AX = B$ and required a nontrivial solution, the determinant of the coefficient matrix must vanish (Timoshenko & Gere, 1989). For a truncated system involving two complete m, n terms, the critical shear load is given by (Timoshenko & Gere, 1989):

$$N_{xy} = \pm \frac{9\,\lambda\,(\beta^2 + 1)^2}{32\,\beta^3} \tag{59}$$

where $\lambda = \frac{\pi^4 D}{b^2}$. It is important to note that the approximation based on only two complete m, n terms yields limited accuracy (Timoshenko & Gere, 1989). As reported by (Timoshenko & Gere, 1989), this simplification introduces an error of approximately 15% for square plates, and the discrepancy becomes more pronounced with increasing aspect ratio. Therefore, for precise evaluation of the critical shear load, high-order terms should be considered, particularly in plates with elongated geometries (Timoshenko & Gere, 1989). The solution with two terms can be written as (Timoshenko & Gere, 1989):

$$N_{xy} = k \frac{\pi^2 D}{b^2} \tag{60}$$

where k is a constant depending on the aspect ratio (β) (Timoshenko & Gere, 1989) (Fig. 26). After the analysis, taking five complete terms, the solution converges to a value of $k = 9.34$ for a square aspect ratio ($\beta = 1$), that is in agreement with the literature from (Timoshenko & Gere, 1989).

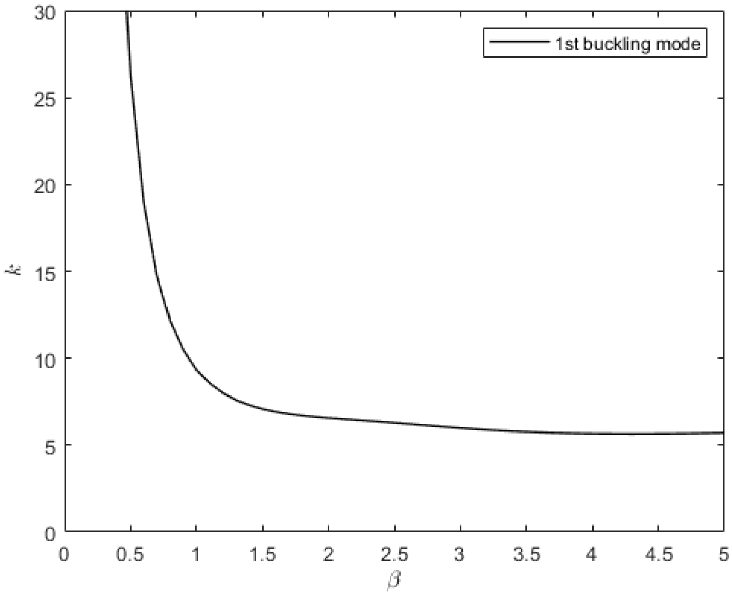

Figure 26: k value for different aspect ratios.

3.4 Buckling of simply supported plate under pure compression with a central hole

According to Figure 27, it is seen two different configurations, a plate with a round central hole, and a plate with a square central hole. By taking the round central perforation, the plate can be subdivided into 4 areas (A_1, A_2, A_3, A_4), setting new integration boundaries. The central circle boundary condition can be written as:

$$y = y_f \pm \sqrt{R^2 - (x - x_f)^2} \tag{61}$$

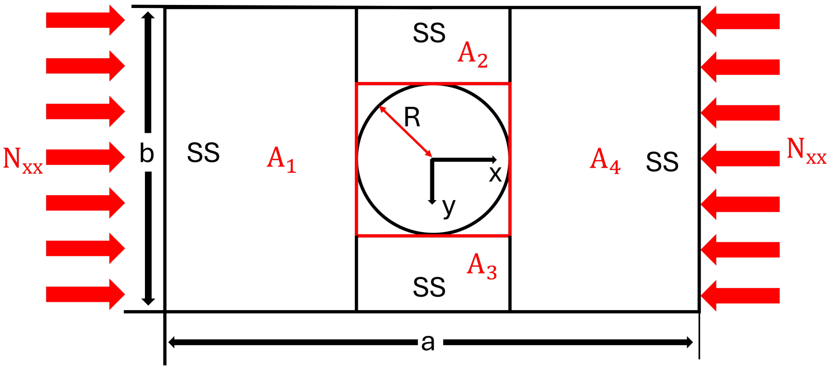

Figure 27: Plate domain subdivided into 4 areas.

This allows to define the boundaries of plate's new domain, where x_f and y_f are the circle center coordinates.
The total strain energy can be written as:

$$U_b = U_{b1} + U_{b2} + U_{b3} + U_{b4} \tag{62}$$

where, each U_{bx} component represents the corresponding plate's subdomain, as seen in Figure 27.

$$U_{b1} = \frac{1}{2}D\int_{-b/2}^{b/2}\int_{-a/2}^{x_f-R}(\frac{\partial^2 w}{\partial x^2})^2 + (\frac{\partial^2 w}{\partial y^2})^2 + 2\nu\frac{\partial^2 w}{\partial x^2}\frac{\partial^2 w}{\partial y^2} + 2(1-\nu)(\frac{\partial^2 w}{\partial x \partial y})^2 dxdy \tag{63}$$

$$U_{b2} = \frac{1}{2}D\int_{-b/2}^{y_f-\sqrt{R^2-(x-x_f)^2}}\int_{x_f-R}^{x_f+R}(\frac{\partial^2 w}{\partial x^2})^2 + (\frac{\partial^2 w}{\partial y^2})^2 + 2\nu\frac{\partial^2 w}{\partial x^2}\frac{\partial^2 w}{\partial y^2} + 2(1-\nu)(\frac{\partial^2 w}{\partial x \partial y})^2 dxdy \tag{64}$$

$$U_{b3} = \frac{1}{2}D\int_{y_f+\sqrt{R^2-(x-x_f)^2}}^{b/2}\int_{x_f-R}^{x_f+R}(\frac{\partial^2 w}{\partial x^2})^2 + (\frac{\partial^2 w}{\partial y^2})^2 + 2\nu\frac{\partial^2 w}{\partial x^2}\frac{\partial^2 w}{\partial y^2} + 2(1-\nu)(\frac{\partial^2 w}{\partial x \partial y})^2 dxdy \tag{65}$$

$$U_{b4} = \frac{1}{2}D\int_{-b/2}^{b/2}\int_{x_f+R}^{a/2}(\frac{\partial^2 w}{\partial x^2})^2 + (\frac{\partial^2 w}{\partial y^2})^2 + 2\nu\frac{\partial^2 w}{\partial x^2}\frac{\partial^2 w}{\partial y^2} + 2(1-\nu)(\frac{\partial^2 w}{\partial x \partial y})^2 dxdy \tag{66}$$

After careful evaluation of the integration limits, due to its complexity, the differential equations of the strain energy and work done by the compressive load, don't have solution. That is, the approach employed was to simplify the circle equation with a *Taylor* series of first order. The consequence of this, is the transformation of a circular boundary condition, into a square or linear boundary condition. With x_f=y_f =0, the circle expression becomes simply the value of R, that is, the circle is approximated into a square (as seen in Figure 27, the second configuration with square central hole). Simplifying the new boundary, the strain energy of the plate becomes:

$$U_{b1} = \frac{1}{2}D\int_{-b/2}^{b/2}\int_{-a/2}^{-R}(\frac{\partial^2 w}{\partial x^2})^2 + (\frac{\partial^2 w}{\partial y^2})^2 + 2\nu\frac{\partial^2 w}{\partial x^2}\frac{\partial^2 w}{\partial y^2} + 2(1-\nu)(\frac{\partial^2 w}{\partial x \partial y})^2 dxdy \quad (67)$$

$$U_{b2} = \frac{1}{2}D\int_{-R}^{R}\int_{-b/2}^{-R}(\frac{\partial^2 w}{\partial x^2})^2 + (\frac{\partial^2 w}{\partial y^2})^2 + 2\nu\frac{\partial^2 w}{\partial x^2}\frac{\partial^2 w}{\partial y^2} + 2(1-\nu)(\frac{\partial^2 w}{\partial x \partial y})^2 dydx \quad (68)$$

$$U_{b3} = \frac{1}{2}D\int_{-R}^{R}\int_{R}^{b/2}(\frac{\partial^2 w}{\partial x^2})^2 + (\frac{\partial^2 w}{\partial y^2})^2 + 2\nu\frac{\partial^2 w}{\partial x^2}\frac{\partial^2 w}{\partial y^2} + 2(1-\nu)(\frac{\partial^2 w}{\partial x \partial y})^2 dydx \quad (69)$$

$$U_{b4} = \frac{1}{2}D\int_{-b/2}^{b/2}\int_{R}^{a/2}(\frac{\partial^2 w}{\partial x^2})^2 + (\frac{\partial^2 w}{\partial y^2})^2 + 2\nu\frac{\partial^2 w}{\partial x^2}\frac{\partial^2 w}{\partial y^2} + 2(1-\nu)(\frac{\partial^2 w}{\partial x \partial y})^2 dxdy \quad (70)$$

The work produced by external forces becomes:

$$V_{TOTAL} = V_1 + V_2 + V_3 + V_4 \quad (71)$$

Since the plate is under compression, only the N_x component will be accounted. This implies that:

$$V_1 = -\frac{1}{2}\int_{-b/2}^{b/2}\int_{-a/2}^{-R} N_x(\frac{\partial w}{\partial x})^2 dxdy \quad (72)$$

$$V_2 = -\frac{1}{2}\int_{-R}^{R}\int_{-b/2}^{-R} N_x\frac{b}{b-2R}(\frac{\partial w}{\partial x})^2 dydx \quad (73)$$

$$V_3 = -\frac{1}{2}\int_{-R}^{R}\int_{R}^{b/2} N_x\frac{b}{b-2R}(\frac{\partial w}{\partial x})^2 dydx \quad (74)$$

$$V_4 = -\frac{1}{2}\int_{-b/2}^{b/2}\int_{R}^{a/2} N_x(\frac{\partial w}{\partial x})^2 dxdy \quad (75)$$

The contribution of the factor presented in equations 73 and 74, allows the work to be distributed accordingly due to missing domain in the center of the plate. The following solution is valid for a plate with a central hole under pure compression, with all simply supported edges (Figure 22 boundary conditions, and with $w(x, y)$ displacement function Equation 44). By employing the energetic method, as seen in the literature, setting a non trivial solution, it is possible to determine several critical buckling loads (for $n = 1$) for different buckling modes ($m = 1, 2, 3, ...$). The critical buckling load ($N_{cr,0}$) expression for the compressed plate with a central hole ($x_f = y_f = 0$) is set as:

$$N_{cr,0} = \frac{\psi_1}{\psi_2} \cdot D \tag{76}$$

where

$$\begin{aligned}
\psi_1 = {} & 8a^3b^4m^3n^3\pi^4 + 4ab^6m^5n\pi^4 - 8Rb^6m^5\pi^3\sigma_1 + 32R^3a^4mn^5\pi^4 \\
& - 16R^2b^5m^5n\pi^4 + 32R^3b^4m^5n\pi^4 + 4a^5b^2mn^5\pi^4 + 16R^2a^5n^5\pi^3\sigma_2 \\
& + 16R^2b^5m^5\pi^3\sigma_1 - 16R^2a^4bmn^5\pi^4 - 4ab^6m^4\pi^2\sigma_2\sigma_1 \\
& - 16Ra^3b^3m^3n^3\pi^4 - 4a^5b^2n^4\pi^2\sigma_2\sigma_1 - 8Rab^5m^5n\pi^4 \\
& - 8Ra^5bmn^5\pi^4 - 32R^2a^2b^3m^3n^3\pi^4 + 64R^3a^2b^2m^3n^3\pi^4 \\
& - 8Ra^5bn^5\pi^3\sigma_2 + 16Ra^3b^3m^2n^3\pi^3\sigma_2 + 16Ra^2b^4m^3n^2\pi^3\sigma_1 \\
& - 8Rab^5m^4n\pi^3\sigma_2 - 8a^3b^4m^2n^2\pi^2\sigma_2\sigma_1 - 32R^2a^3b^2m^2n^3\pi^3\sigma_2 \\
& - 32R^2a^2b^3m^3n^2\pi^3\sigma_1 + 8Rab^5m^4\pi^2\sigma_2\sigma_1 + 8Ra^5bn^4\pi^2\sigma_2\sigma_1 \\
& + 16R^2ab^4m^4n\pi^3\sigma_2 - 8Ra^4b^2mn^4\pi^3\sigma_1 + 16R^2a^4bmn^4\pi^3\sigma_1 \\
& - 32Ra^3b^3m^2n^3\nu\pi^3\sigma_2 - 32Ra^2b^4m^3n^2\nu\pi^3\sigma_1 \\
& + 16Ra^3b^3m^2n^2\pi^2\sigma_2\sigma_1 + 64R^2a^3b^2m^2n^3\nu\pi^3\sigma_2 \\
& + 64R^2a^2b^3m^3n^2\nu\pi^3\sigma_1
\end{aligned}$$

$$\psi_2 = 4a^3b^6m^3n\pi^2 + 4a^3b^6m^2\sigma_2\sigma_1 - 8Ra^3b^5m^3n\pi^2 - 8\pi Ra^2b^6m^3\sigma_1$$

and where

$$\begin{aligned}
\sigma_1 &= \sin\left(\frac{2\pi Rn}{b}\right), \\
\sigma_2 &= \sin\left(\frac{2\pi Rm}{a}\right).
\end{aligned}$$

With equation 76, it is possible to obtain the global buckling coefficient (k_g), being:

$$k_g = \frac{N_{cr,0} b^2}{\pi^2 D}$$

$$k_g = \frac{(2R - b) \cdot \psi_3}{\psi_4} \tag{77}$$

where

$$\begin{aligned}\psi_3 = 8\pi R a^5 n^5 \sigma_2 &- 8a^3 b^3 m^3 n^3 \pi^2 + 8\pi R b^5 m^5 \sigma_1 - 4ab^5 m^5 n \pi^2 \\ &- 4a^5 bmn^5 \pi^2 + 4ab^5 m^4 \sigma_2 \sigma_1 + 4a^5 bn^4 \sigma_2 \sigma_1 \\ &+ 16R^2 a^4 mn^5 \pi^2 + 16R^2 b^4 m^5 n \pi^2 + 8a^3 b^3 m^2 n^2 \sigma_2 \sigma_1 \\ &+ 32R^2 a^2 b^2 m^3 n^3 \pi^2 + 8\pi R a b^4 m^4 n \sigma_2 + 8\pi R a^4 bmn^4 \sigma_1 \\ &- 16\pi R a^3 b^2 m^2 n^3 \sigma_2 - 16\pi R a^2 b^3 m^3 n^2 \sigma_1 \\ &+ 32\pi R a^3 b^2 m^2 n^3 \nu \sigma_2 + 32\pi R a^2 b^3 m^3 n^2 \nu \sigma_1\end{aligned}$$

$$\psi_4 = a^2 b^3 m^2 \big(4ab\sigma_2 \sigma_1 - 8\pi R bm \sigma_1 - 8Ramn\pi^2 + 4abmn\pi^2\big)$$

4 Numerical development

Several numerical parametric analysis were carried in order to evaluate the influence of different cutout diameters in several aspect-ratios. The input parameters are only geometrical, in order to set a cutout diameter and evaluate its influence for different aspect-ratios. Such parameters are the d_f/b, β, and b. The numerical setup and boundary conditions applied can be seen in Figure 28 and Table 5. This setup is for a general plate with a central circular perforation, with all borders simply supported, and a distributed compressive load (N_{xx}) is applied on both vertical borders in the x direction.

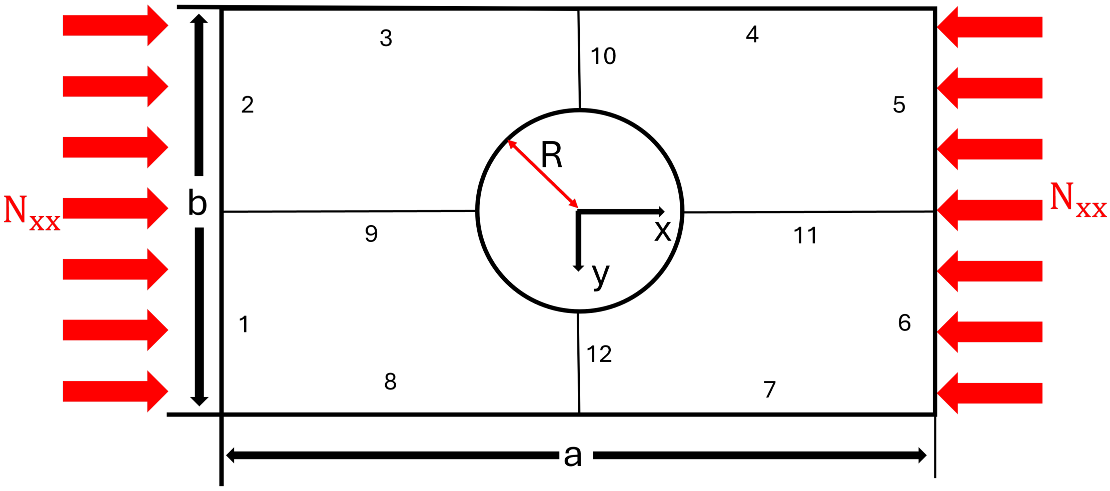

Figure 28: Numerical setup used in finite element analysis.

Table 5: Numerical model boundary conditions.

Edge	DOF	Edge	DOF
1	w=0	7	w=0
2	w=0	8	w=0
3	w=0	9	v=0
4	w=0	10	u=0
5	w=0	11	v=0
6	w=0	12	u=0

As for the parameters, Table 6, shows all the combinations made for this analysis.

Table 6: Parameters for plate analysis.

Parameter	Range
d_f/b	[0;0.8]
β	[0.1;5.0]

4.1 Mesh convergence analysis

To determine the ideal mesh element size, a mesh sensibility analysis is performed to a perforated square plate using the boundary conditions from Table 5 and loading scheme from Figure 28. To control the mesh, the plate surface is subdivided in several regions (Figure 29), guarantying mesh continuity, and stabilizing all the element size divisions. The chosen start value of $50mm$, is the minimum possible to guarantee the edges division.

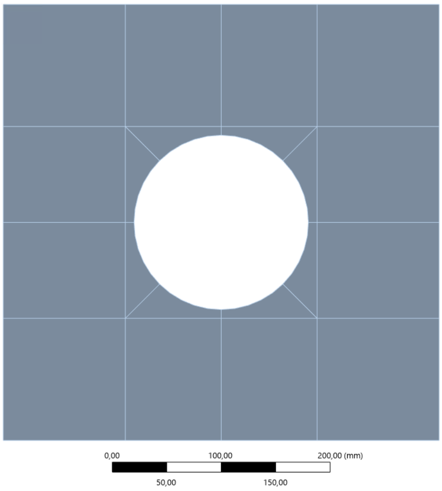

Figure 29: Square plate model $\beta = 1$, with $d_f/b = 0.4$ face divisions.

From Figure 30, there is almost no difference between the solutions when the element size is $10mm$ compared to the $5mm$ solution. The ideal mesh size will be set as $5mm$.

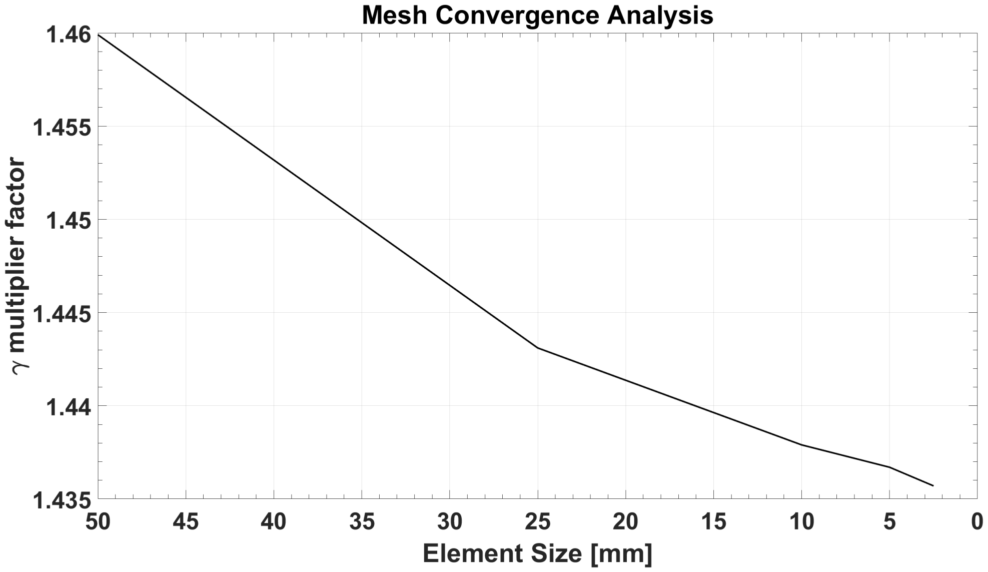

Figure 30: Mesh convergence analysis for different element sizes.

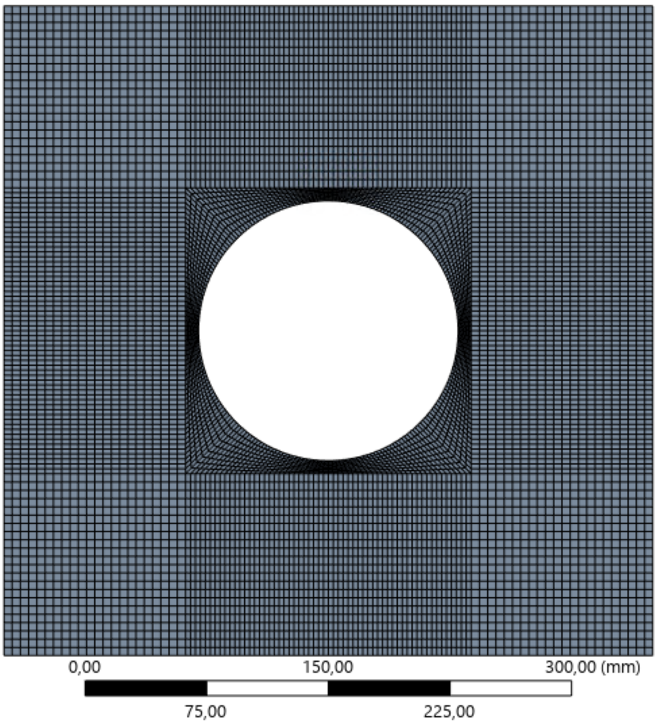

Figure 31: Square plate model $\beta = 1$, with $d_f/b = 0.4$ generated mesh.

Numerical simulations in structural analysis frequently employ finite element methods to model complex geometries and behaviors. Among the available tools, *ANSYS* has been widely used for its robust simulation capability. For this case of study, *SHELL181* element was used, where it has four nodes (nodes I, J, K, and L), featuring six degrees of freedom at each node (translations along X, Y, and Z axes, as well as rotations about these axes) (ANSYS, 2024). The versatility of *SHELL181* is further enhanced by its configurable options. When the membrane option is enabled, the element simplifies to include only translational degrees of freedom, making it suitable for specific membrane applications (ANSYS, 2024). Also, the degenerate triangular form of *SHELL181*, should be used only as filler elements during mesh generation (ANSYS, 2024). The geometric configuration, node placement, and orientation of this element are illustrated in Figure 32, giving a visual reference for its implementation in simulation workflows (ANSYS, 2024).

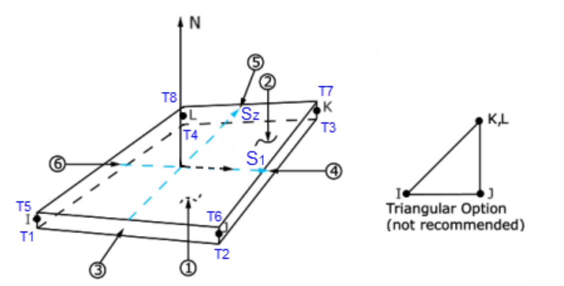

Figure 32: SHELL181 Geometry ANSYS, 2024

This element is particularly well suited for a range of structural analysis applications, including linear, large rotation, and large strain non linear problems (ANSYS, 2024). Its formulation includes changes in shell thickness during non-linear analyses, enhancing its applicability to complex deformation scenarios (ANSYS, 2024). Within the element domain, both full and reduced integration schemes are supported, offering flexibility in balancing computational efficiency and accuracy (ANSYS, 2024). Also, this element is employed for layered applications, as illustrated in Figure 33, making it an effective choice for modeling composite shells and sandwich constructions. (ANSYS, 2024). The accuracy of such simulations is governed by the first order shear deformation theory, commonly referred to as the Mindlin-Reissner shell theory, which accounts for the transverse shear effects and enhances the accuracy of composite shell modeling (ANSYS, 2024).

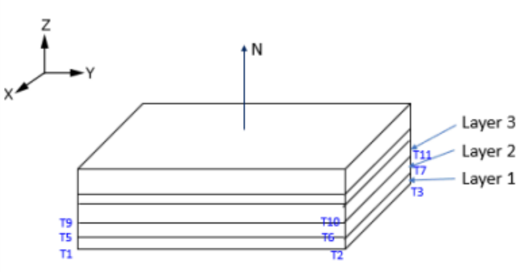

Figure 33: Layered construction SHELL181 ANSYS, 2024

The stiffness-matrix of this element (Figure 34) is governed by the shape functions (Eq. 78) for 3D 4-node quadrilateral shells (ANSYS, 2024):

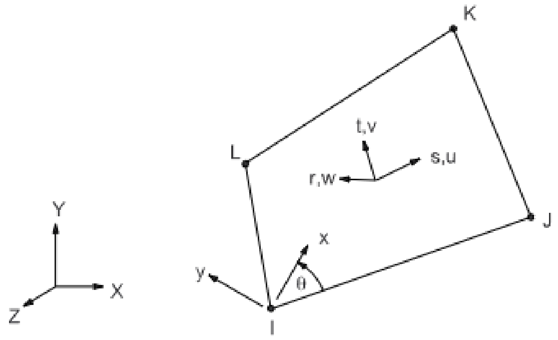

Figure 34: SHELL181 node scheme ANSYS, 2024

$$
\begin{aligned}
u &= \frac{1}{4}(u_I(1-s)(1-t) + u_J(1+s)(1-t) + u_K(1+s)(1+t) + u_L(1-s)(1+t)) \\
v &= \frac{1}{4}(v_I(1-s)(1-t) + v_J(1+s)(1-t) + v_K(1+s)(1+t) + v_L(1-s)(1+t)) \\
w &= \frac{1}{4}(w_I(1-s)(1-t) + w_J(1+s)(1-t) + w_K(1+s)(1+t) + w_L(1-s)(1+t)) \\
\theta_X &= \frac{1}{4}(\theta_{XI}(1-s)(1-t) + \theta_{XJ}(1+s)(1-t) + \theta_{XK}(1+s)(1+t) + \theta_{XL}(1-s)(1+t)) \\
\theta_Y &= \frac{1}{4}(\theta_{YI}(1-s)(1-t) + \theta_{YJ}(1+s)(1-t) + \theta_{YK}(1+s)(1+t) + \theta_{YL}(1-s)(1+t))
\end{aligned}
\tag{78}
$$

4.2 Numerical model validation

Describing the numerical model from (El-Sawy & Nazmy, 2001), it is a typical plate, with length (a), width (b), and circular eccentric hole with diameter (d) (Figure 35).

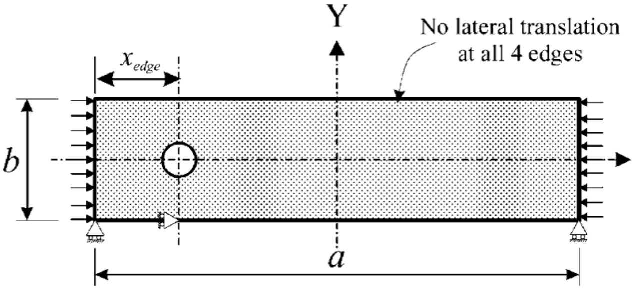

Figure 35: Numerical model used by (El-Sawy & Nazmy, 2001).

The boundary conditions for the plate edges are simply supported in the out of plane direction, and 3 points are restrained to prevent in-plane motion (avoiding rigid body movement). An uniform load is applied perpendicular to the short edges (N_{xx}). As for mesh control, two criteria are applied: (i) default element size all over the plate is $b/20$; (ii) element size along the hole perimeter is smaller of $b/50$ or $\pi d/40$;.

To validate the present numerical model, two sets of tests were conducted and compared with (El-Sawy & Nazmy, 2001) numerical simulations (Figures 36, and 37).

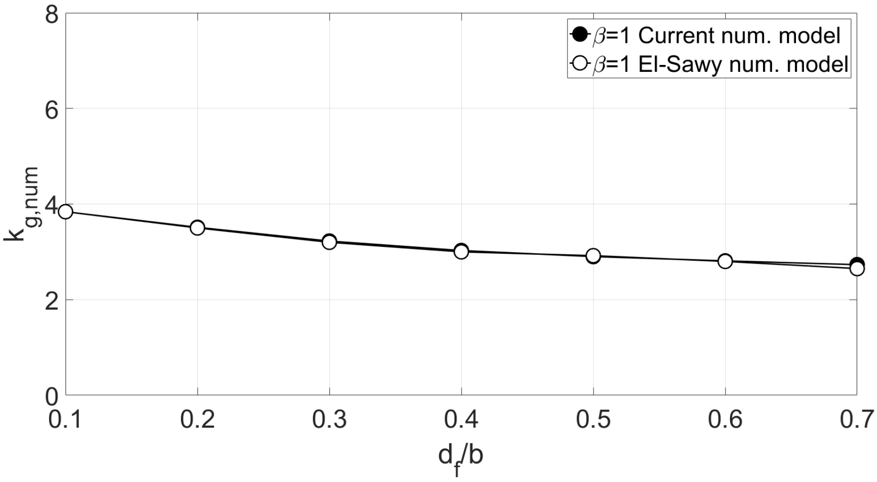

Figure 36: Comparison between current numerical model, and (El-Sawy & Nazmy, 2001) numerical solution for an aspect ratio of $\beta = 1$.

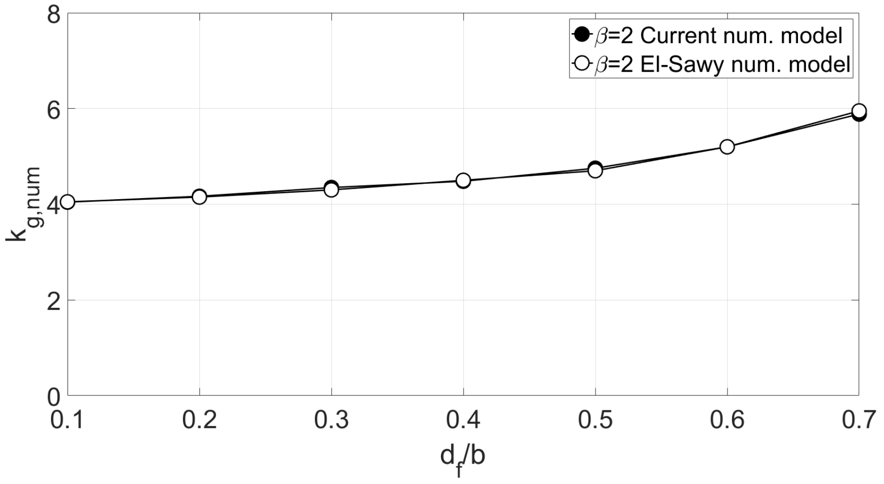

Figure 37: Comparison between current numerical model, and (El-Sawy & Nazmy, 2001) numerical solution for an aspect ratio of $\beta = 2$.

Table 7 provides the global buckling factors from the current numerical model ($k_{g,num,cur}$), and (El-Sawy & Nazmy, 2001) global buckling factors ($k_{g,num,El-Sawy}$). The relative error between solution is negligible ($\leq 5\%$), and the difference is due to the mesh configuration, validating the accuracy of the numerical model used in this study.

Table 7: Numerical model validation

β	x_e/b	d_f/b	y_e/b	$k_{g,num,cur}$	$k_{g,num,El-Sawy}$	Relative Error (%)	Ref.
1	0.5	0.1	0.45	3.85	3.84	0.26	(El-Sawy & Nazmy, 2001)
		0.2	0.40	3.50	3.57	2.00	
		0.3	0.35	3.20	3.23	0.94	
		0.4	0.30	3.00	3.03	1.00	
		0.5	0.25	2.92	2.90	0.68	
		0.6	0.20	2.80	2.81	0.36	
		0.7	0.15	2.65	2.73	3.02	
2	1	0.1	0.45	4.05	4.04	0.25	(El-Sawy & Nazmy, 2001)
		0.2	0.40	4.15	4.17	0.48	
		0.3	0.35	4.30	4.35	1.16	
		0.4	0.30	4.50	4.48	0.44	
		0.5	0.25	4.70	4.75	1.06	
		0.6	0.20	5.20	5.20	0.00	
		0.7	0.15	5.95	5.88	1.18	

4.3 Elastic Buckling analysis

Using a finite element approach, numerical simulations were carried evaluating critical parameters, such as the aspect-ratio β, and the perforation diameter d_f. Within the scope of this study, it is important to perform an analysis to evaluate whether the yield will occur due to elastic instability or by plastic yielding. Figure 38, clearly show that a solid plate under compression with a slenderness ($b/t_w \leq 60$), yielding will occur by plastic yield. In contrast, above the mentioned slenderness, the yielding will be by buckling instability, below the values of elastic stress limit.

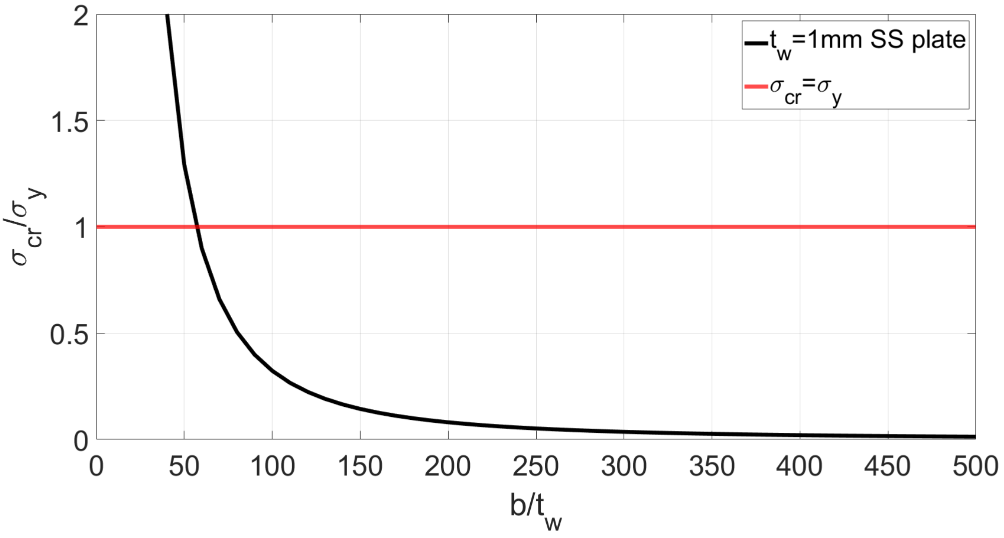

Figure 38: Slenderness sensibility analysis for a simply supported plate on all borders, with a thickness of $1mm$.

The following study carried all the numerical analysis, with a plate simply supported on all borders, with a slenderness of 400. A parametric analysis is made regarding the aspect-ratio, and hole diameter ratio, evaluating its non-dimensional buckling coefficient ($k_{f,num}$), in which:

$$k_{f,num} = \frac{k_{g,num}}{k_{num,solidplate}} \tag{79}$$

Setting an *Eigenvalue* analysis, it is possible to determine the load from which the buckling occurs ($N_{cr0,num}$) for several modes of instability. The value of ($k_{f,num}$) is obtained for each diameter ratio (Figure 39).

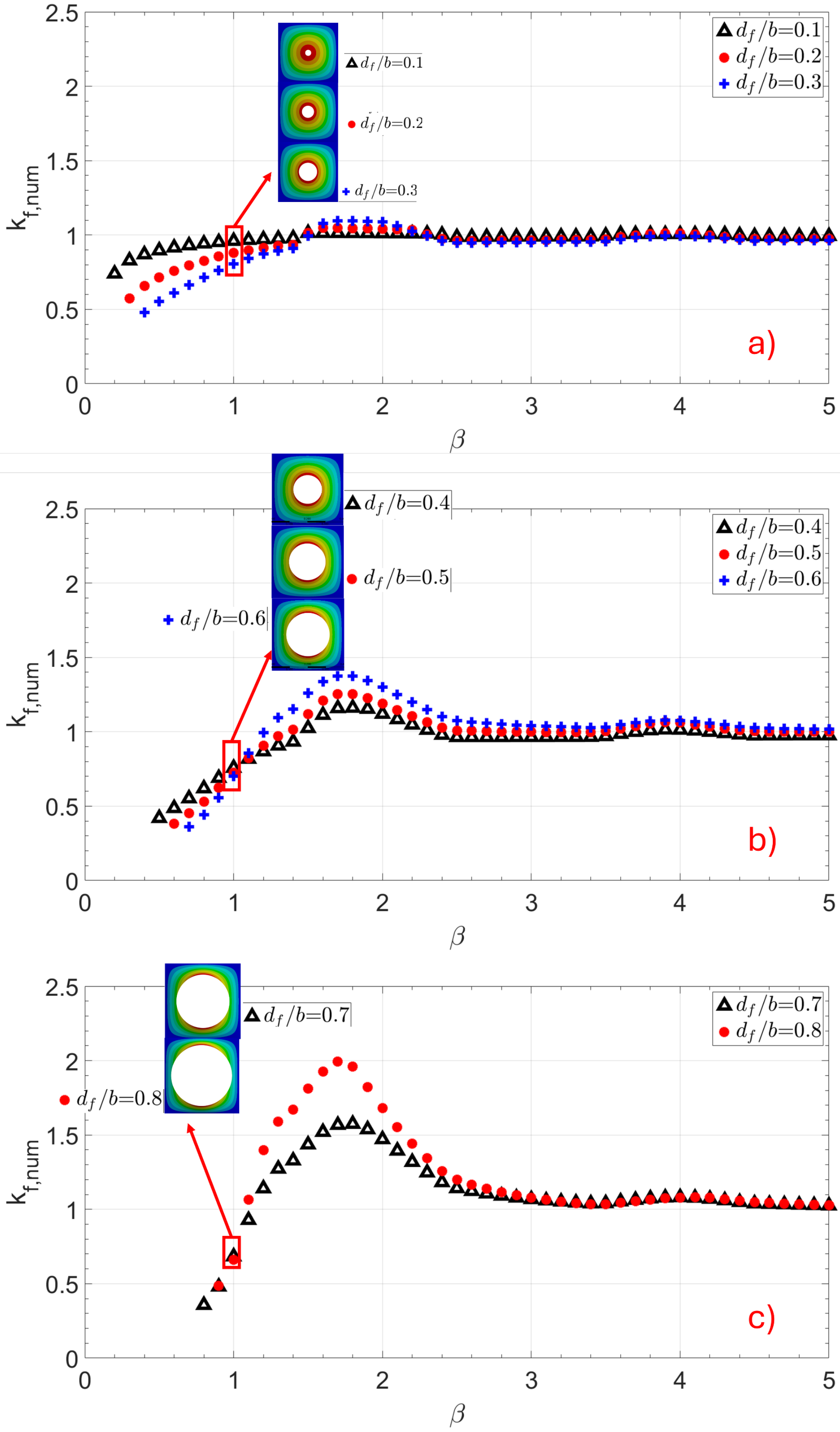

Figure 39: Non-dimensional buckling coefficients $k_{f,num}$ for plates with central perforation: $a)$ $0.1 \leq d_f/b \leq 0.3$; $b)$ $0.4 \leq d_f/b \leq 0.6$; $c)$ $0.7 \leq d_f/b \leq 0.8$;.

5 Experimental development

For more accurate data, an experimental setup was develop to analyze the compressive critical buckling load of solid or alveolar plates, as to compare with numerical and analytical procedures already presented. This setup, aims to replicate several boundary conditions, as all borders simply supported, clamped, or a mixture of both (Figure 40). The Bill of Materials, as the 2D drawings for building and assembly the setup is present in Appendix A. The plate is placed with the length (a) parallel to the load direction (Figure 41). The specimens are listed on Table 8.

Table 8: Specimen list for experimental procedure.

Specimen	β	d_f/b	t_w	Material
P1.5β1.1	1.1	0	1.5	S235JR
P1.5β1.5	1.5	0	1.5	S235JR

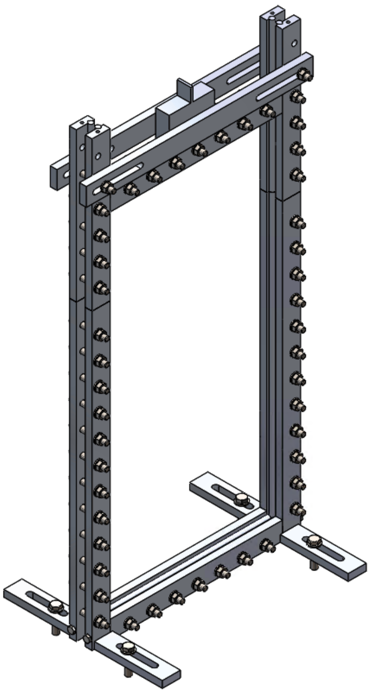

Figure 40: CAD of experimental setup for plates under compression.

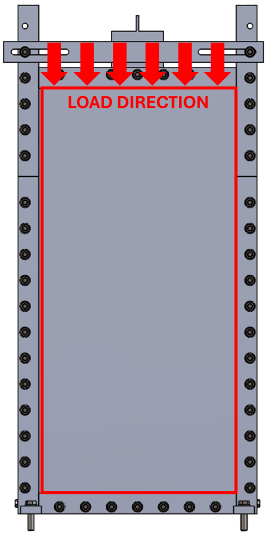

Figure 41: Plate positioning for experimental analysis.

5.1 Setup

This device was developed to be assembled in a general tensile/compression testing machine. Regarding instrumentation, the first step is to obtain/calibrate the experimental procedures with a reference solid plate. The out-of-plane deflection during the compressive test is recorded using two Linear Variable Displacement Transducers (LVDTs) placed at the center of the plate on both sides (Figure 42). Regarding setup parameters, the cross head speed was set as $1mm/min$.

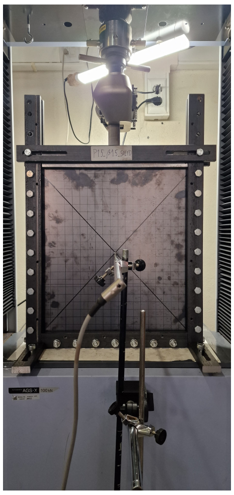

Figure 42: Instrumentation of the solid plate specimens.

5.2 Material characterization

In order to evaluate the material mechanical properties, a tensile test was performed. The material used in the experimental procedures is S235JR steel with a thickness of $1.5mm$. Material characterization was made in agreement of ISO6892-1:2009, both engineering and true stress/strain curves, can be seen in Figures 44 and 45. All tests were validated, since the rupture occurred inside the rupture zone.

Figure 43: Specimens for material characterization: a) Specimens preparation; b) Specimen during test; c) Specimen final results;.

The average curve from Figure 45 was built with all the 7 specimens experimental data, and the yield stress value was $\sigma_y = 264.837MPa$, and ultimate stress was $\sigma_u = 353.259MPa$, with a standard deviation of $2.692MPa$ and $3.259MPa$ respectively.

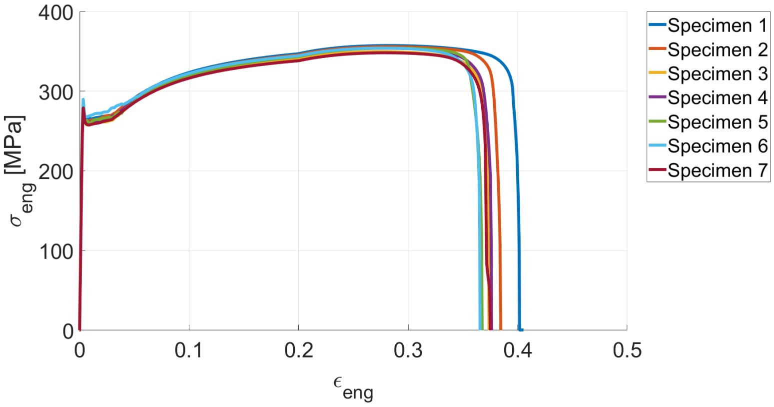

Figure 44: Engineering stress/strain curve.

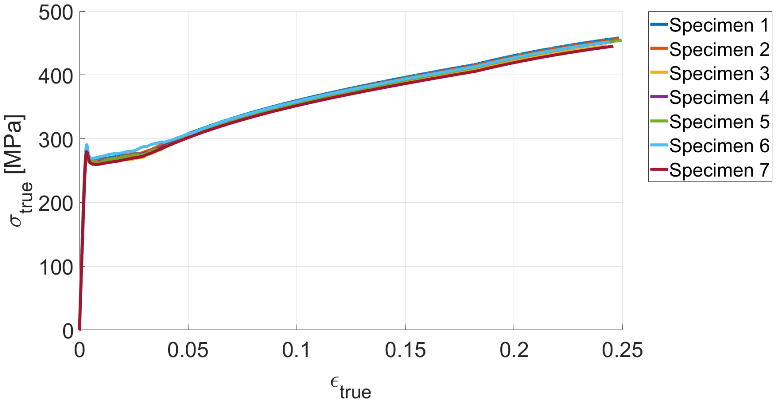

Figure 45: True stress/strain curve.

5.3 Results and comments

Combining the data provided by the LVDT and the load provided by the general tensile/compression machine, it is possible to build a graphic were force and lateral displacement are related. With this analysis it is possible to identify the value of the buckling load, and the collapse load. The results can be in Figure 46, and Figure 47. It is evident from Figure 46, that there is a sudden movement of the plate happening bellow $5000N$, which is expected, revealing the buckling load. This phenomena is much more pronounced if the plate has less lateral imperfections.

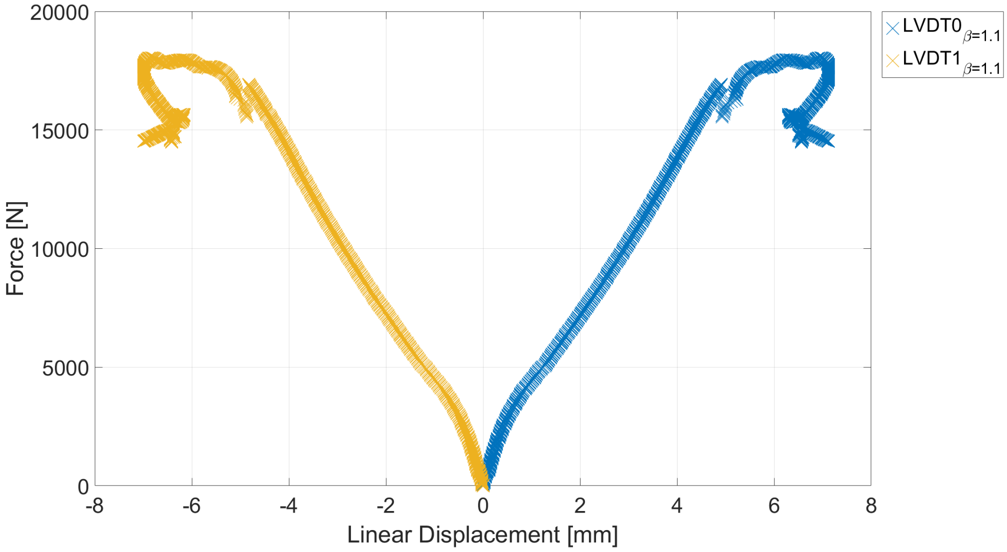

Figure 46: Experimental result of compression test with force vs lateral displacement for specimen $P1.5\_\beta1.1\_SOLID$.

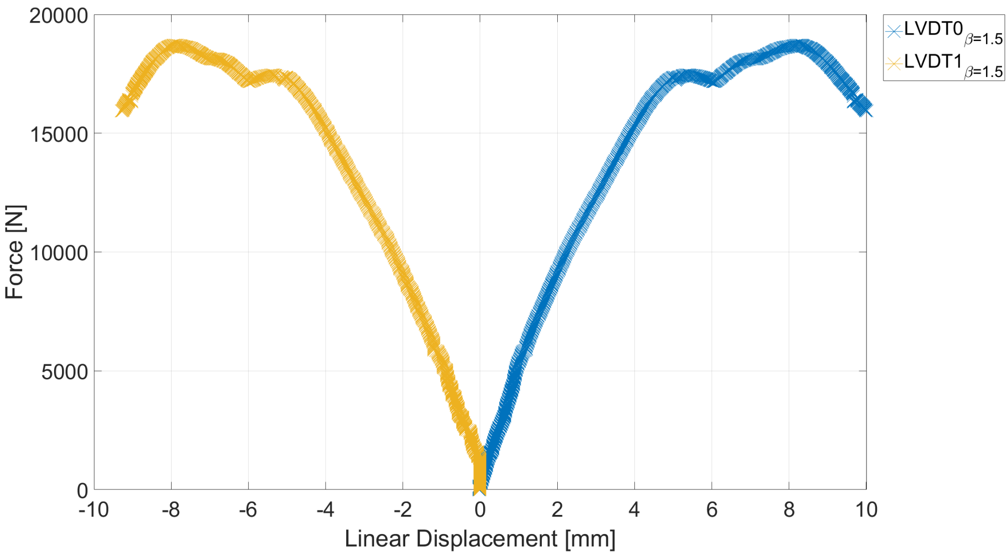

Figure 47: Experimental result of compression test with force vs lateral displacement for specimen $P1.5\_\beta1.5\_SOLID$.

6 Discussion and results

In this section, two solutions will be presented and analyzed: one set of equations valid for specific values of β, that will depend on the d_f/b ratio; a general equation, valid for $1 \leq \beta \leq 4$, that depends on on β and d_f/b ratio. The objective is to obtain an explicit coefficient $k_{f,app.}$ in order to maintain the practical closed form expression as:

$$N_{cr,h} = k_{f,app.} k_s \frac{\pi^2 D}{b^2} \tag{80}$$

From Figure 48, the scattered points of d_f/b ratios, are much more positioned in the bottom right corner of the graph. This implies that, the analytical solution is not being representative of the numerical solution (also seen in Figures 49,50,51, and 52). The analytical non dimension buckling coefficient ($k_{f,ana}$) provided in Figure 48, is being retrieved as the minimum value associated to the m value being calculated, guarantying that the lowest value of this buckling factor is being calculated. This also indicates that the analytical solution is not sensible by the shifting of buckling mode, when larger ratios of d_f/b are used.

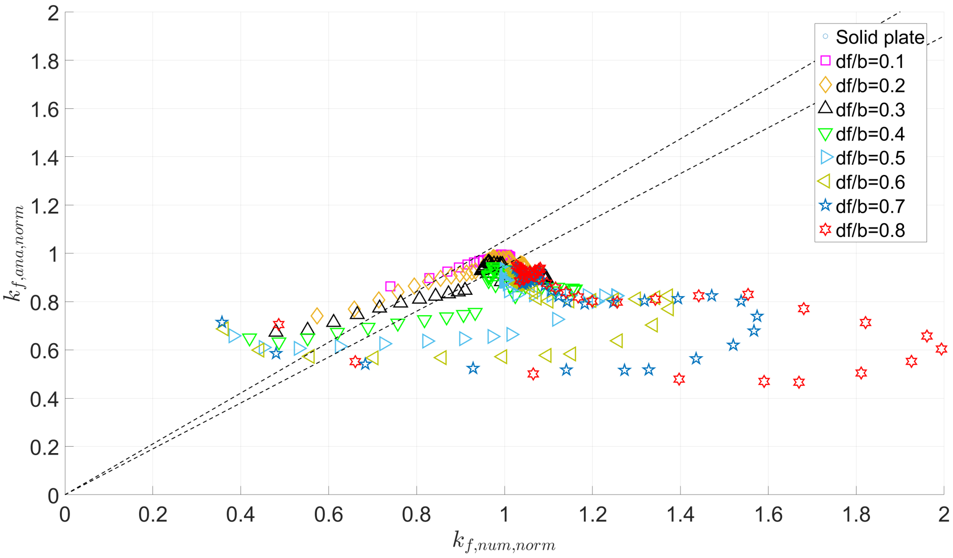

Figure 48: $k_{f,ana,norm}$ (retrieving the minimum value of $k_{f,ana}$ associated with m value) vs $k_{f,num,norm}$, with an error limit of 5%.

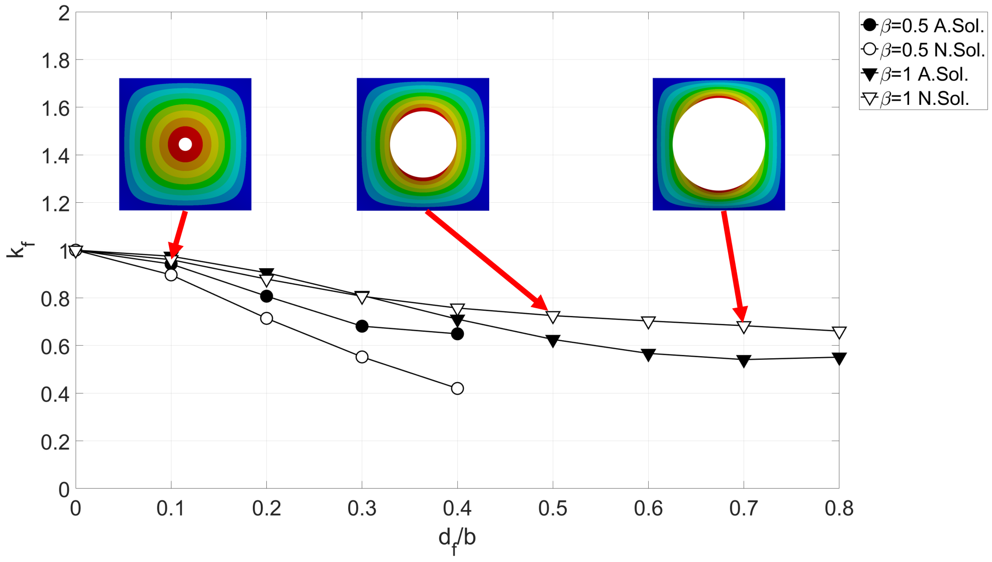

Figure 49: Values of k_f under the influence of the radius cutout for different aspect-ratios.

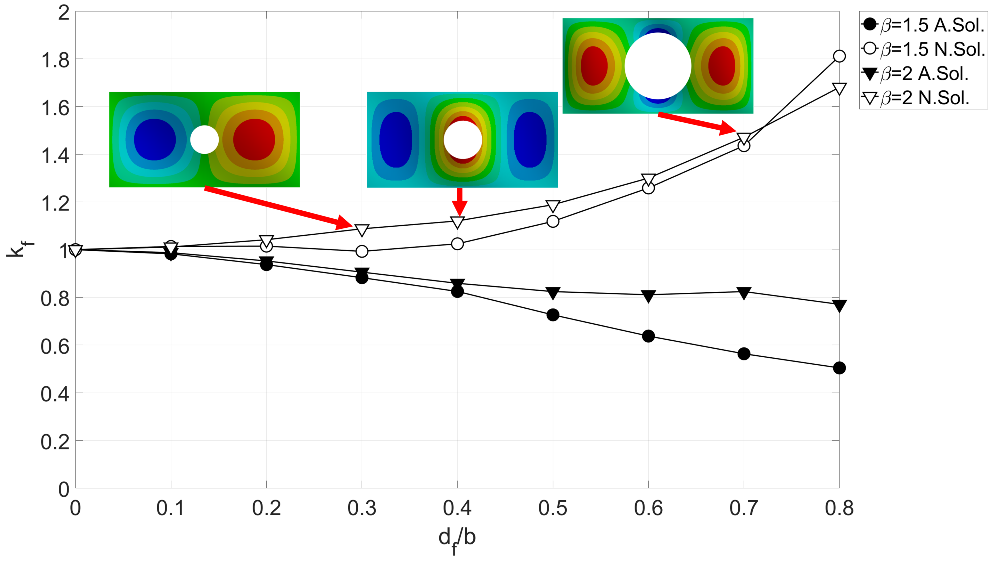

Figure 50: Values of k_f under the influence of the radius cutout for different aspect-ratios.

For $\beta = 2$ (Figure 50), as the ratio increases there is a buckling resistance gain. Due to the physical dimensions of the plate, this unique value of β, as the ratio increases, shifting to an higher buckling mode cannot be made, and before reaching it will yield.

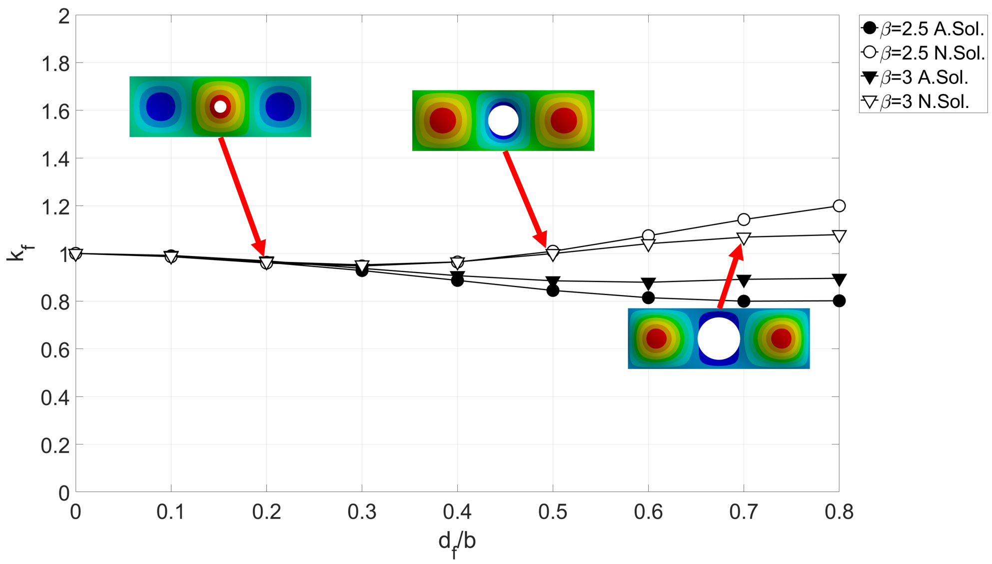

Figure 51: Values of k_f under the influence of the radius cutout for different aspect-ratios. taylored

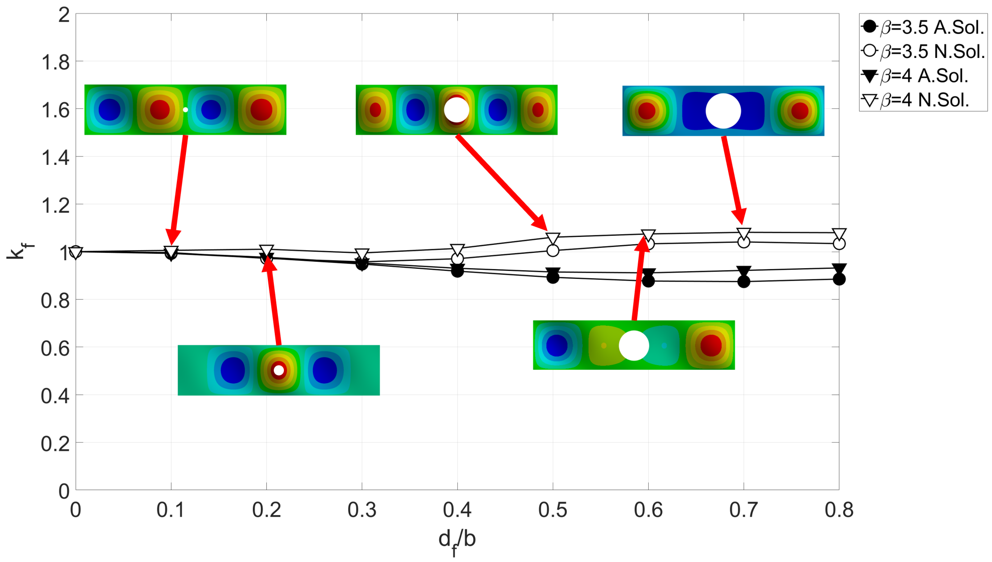

Figure 52: Values of k_f under the influence of the radius cutout for different aspect-ratios. taylored

Considering the buckling shape of the plate, nodal cross lines act as imaginary supports for the lateral direction, and the resistance to buckling is provided by the bending stiffness of the plate portion between these nodal cross lines (El-Sawy & Nazmy, 2001). As the hole size increases beyond a critical point, the local plate bending stiffness at the cross line decreases allowing it to move laterally, changing the buckling mode (El-Sawy & Nazmy, 2001). When the center of the perforation lies on the major axis of the plate at a point of maximum amplitude (Figure 10), it is seen that square plates show the worst stability as the hole size increases, followed by the rectangular plates with the perforation located in the center of the end panel (El-Sawy & Nazmy, 2001). When the hole lies in the center of end panel (over a maximum amplitude cross line), the buckling coefficient k decreases, implying that the largest resistance to buckling is provided by the bending stiffness of the middle portion of the plate (El-Sawy & Nazmy, 2001). On inverse trend, when the center of the hole lies in the center of an interior panel of a rectangular plate, more resistance to buckling is provided from the panels at both sides of the perforated one (El-Sawy & Nazmy, 2001). The buckling behavior of square plates, deviates completely from the rectangular ones (El-Sawy & Nazmy, 2001). From Figure 53, the positioning of nodal and cross lines at maximum amplitude for each aspect ratio applied to solid plates, it is applied for perforated plates as well. The analytical solution cannot consider the gain of resistance provided by the adjacent plates, and this buckling mode shifting, leading to a lower values of k_g.

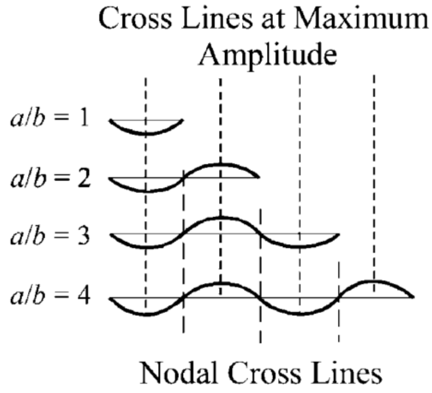

Figure 53: Fundamental buckling mode for solid plates with different integer aspect ratios (El-Sawy & Nazmy, 2001).

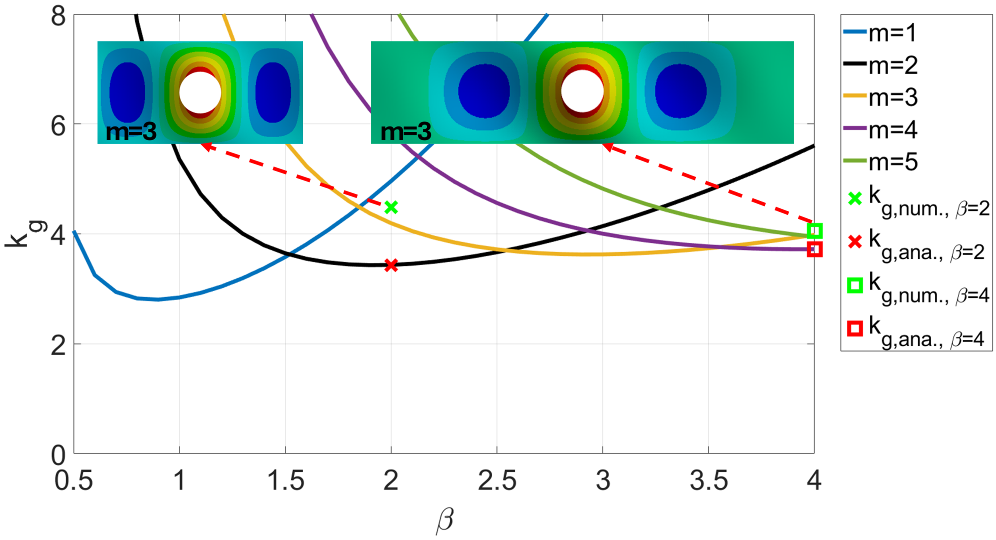

Figure 54: Comparison of global buckling coefficients ($d_f/b = 0.4$) and corresponding mode m given from numerical solution and analytical methodology.

Figures 54, and 55 represent the values of global buckling coefficients for two specific cases of d_f/b ratio. Clearly, the lowest value of k_g from the analytical solution, is given by the buckling mode $m = 2$ (case Figure 54, $\beta = 2$), which does not agree with the corresponding buckling mode from the numerical solution. For the given d_f/b ratio and plate configuration, the first buckling mode to happen is $m = 3$, and not $m = 2$ given by the analytical solution. Same happens for $\beta = 4$, where analytical solution provides $m = 4$ and numerical solution gives $m = 3$.

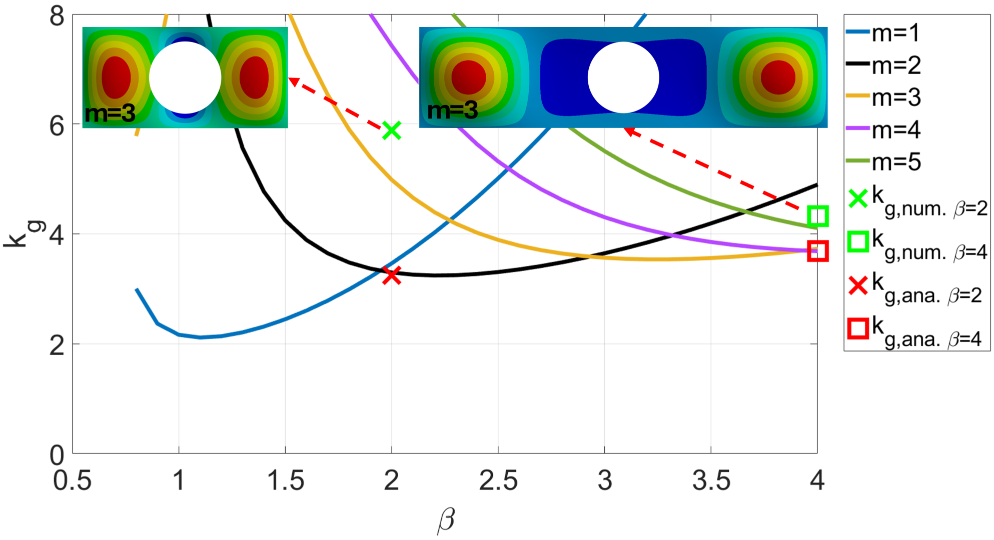

Figure 55: Comparison of global buckling coefficients ($d_f/b = 0.7$) and corresponding mode m given from numerical solution and analytical methodology.

With increasing value of d_f/b, the buckling mode for both cases remain the same, and it is only valid for these unique values of β with these diameter ratios. This implies that, even for rectangular plates, there are specific cases, such as $\beta = 2$. After reaching a critical value of β, the trend is the same, that is, for larger values of β, the hole diameter does not influence the buckling factor k_g, even with the buckling mode changing to higher values. For the analyzed cases, the relation between aspect ratio and hole diameter ratios is presented in Table 9.

Table 9: Numerical buckling modes based on β and d_f/b conditions.

β	Condition	m_{num}
Even (except $\beta = 2$)	$d_f/b = 0.1$	$m = \beta$
	$d_f/b = 0.6$	$m = \beta$
	$d_f/b = 0.5$[1]	$m = \beta + 1$
	$0.2 \leq d_f/b \leq 0.4$	$m = \beta - 1$
	$0.7 < d_f/b \leq 0.8$	$m = \beta - 1$
Odd	$0.1 \leq d_f/b \leq 0.8$	$m = \beta$
$\beta = 2$	$0.1 \leq d_f/b < 0.4$	$m = \beta$
	$d_f/b \geq 0.4$	$m = \beta + 1$

---

[1] Valid only for $\beta = 4$.

Taking all this into consideration, it is not reasonable, neither adequate, to use the analytical solution, when trying to explicit derive approximated equations. From herein, only the numerical solutions (*Eigenvalue* buckling), will be considered for approximation. Equations developed are based on the non dimension bucking factor k_f methodology, respecting the closed format of Equation 80. Table 10, provides all the coefficients needed to build all equations. Solution plot of different non dimensional approximate buckling factors ($k_{f,app.}$) can be seen in Figures 56 to 63.

$$k_{f,app.}(\frac{d_f}{b}) = \sum_{i=0} \alpha_i (\frac{d_f}{b})^i \tag{81}$$

Table 10: Coefficients α_i for different values of β.

β	α_0	α_1	α_2	α_3	α_4	α_5	α_6
0.5	1	-1.2948	-0.4553	0	0	0	0
1	1	-0.7317	0.3861	0	0	0	0
1.5	1	0	-0.8968	2.6646	0	0	0
2	1	-0.1932	1.2549	0	0	0	0
2.5	1	-0.3813	0.8072	0	0	0	0
3	1	0	-1.7965	5.4945	-3.8740	0	0
3.5	1	0	-1.9440	7.2379	-7.9529	2.5281	0
4	1	0	2.4409	-23.2099	76.1930	-100.5586	46.3251

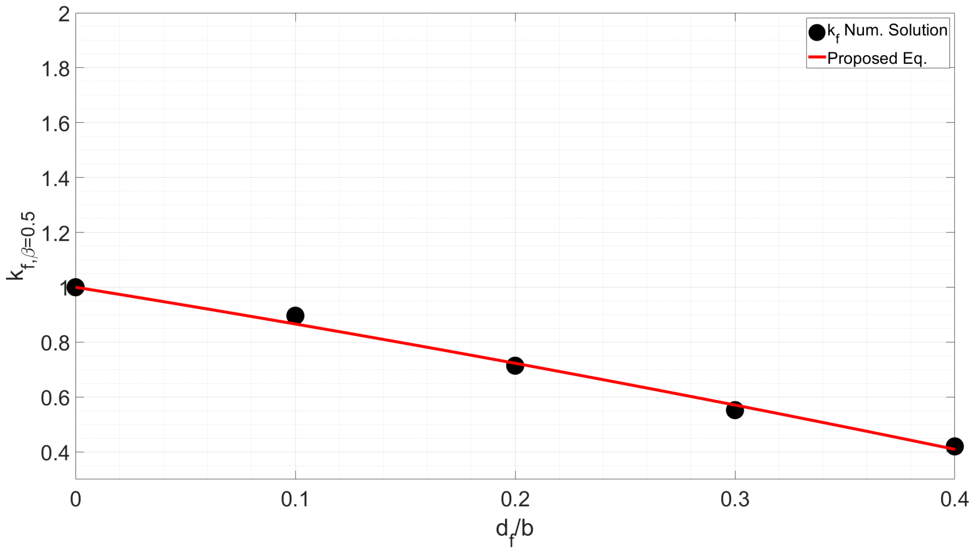

Figure 56: Fit equation of $k_{f,app.,\beta=0.5}$, with a determination factor $R^2 = 0.99362$

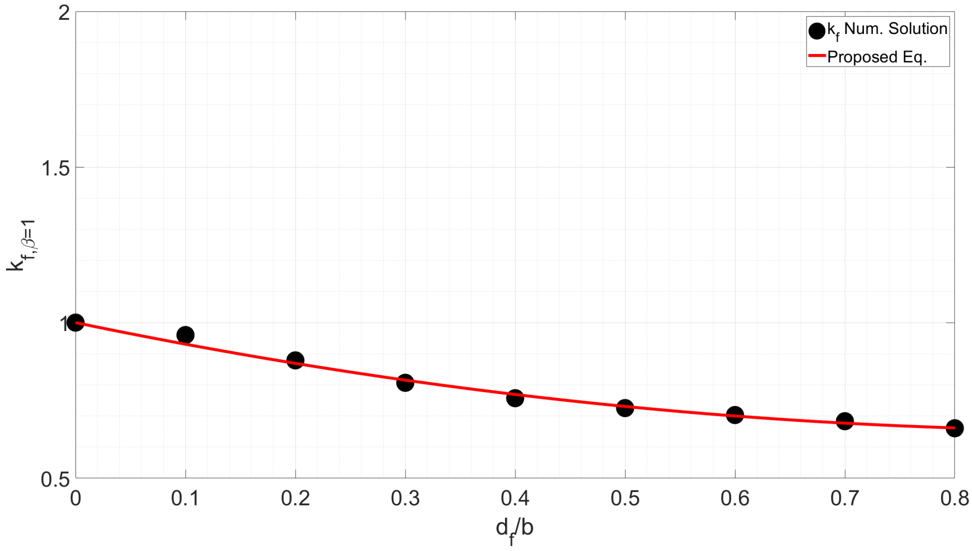

Figure 57: Fit equation of $k_{f,app.,\beta=1}$, with a determination factor $R^2 = 0.98972$

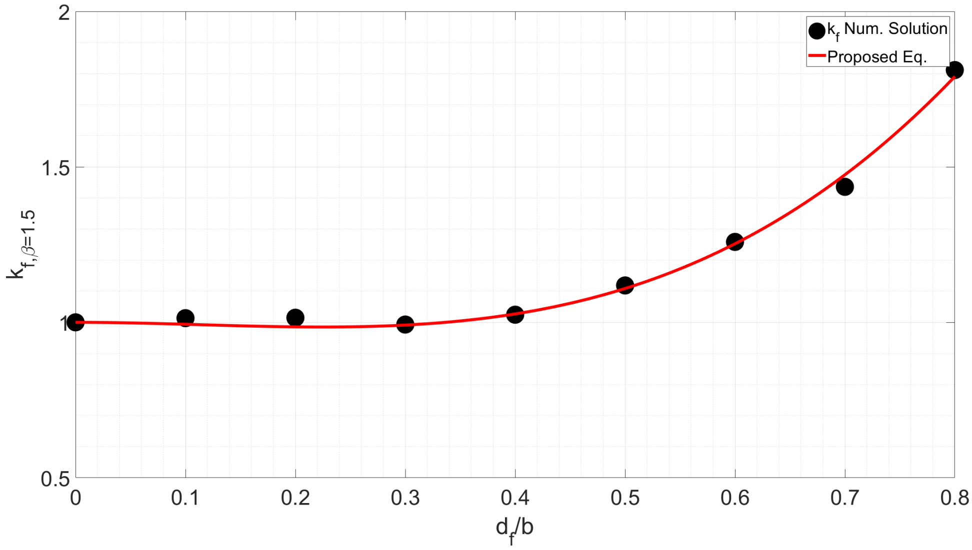

Figure 58: Fit equation of $k_{f,app.,\beta=1.5}$, with a determination factor $R^2 = 0.99463$

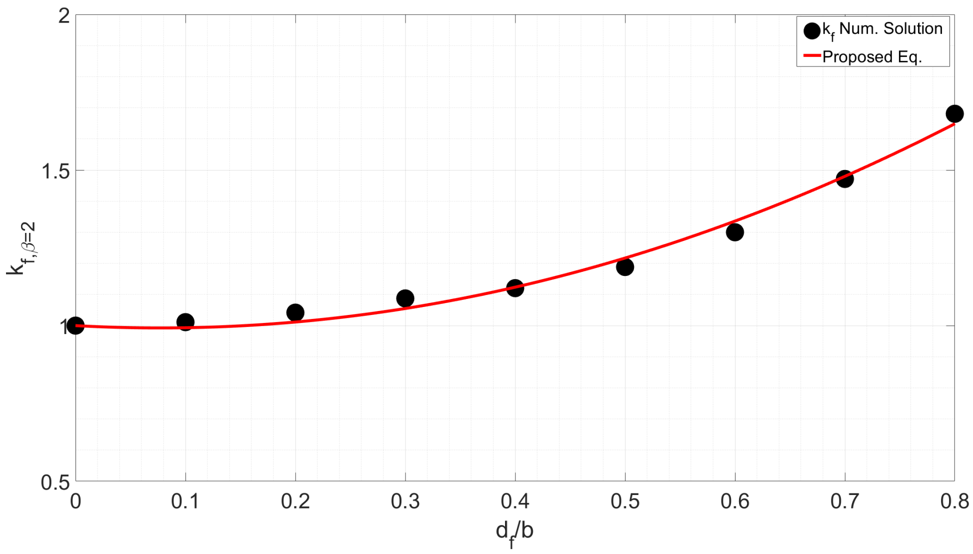

Figure 59: Fit equation of $k_{f,app.,\beta=2}$, with a determination factor $R^2 = 0.98731$

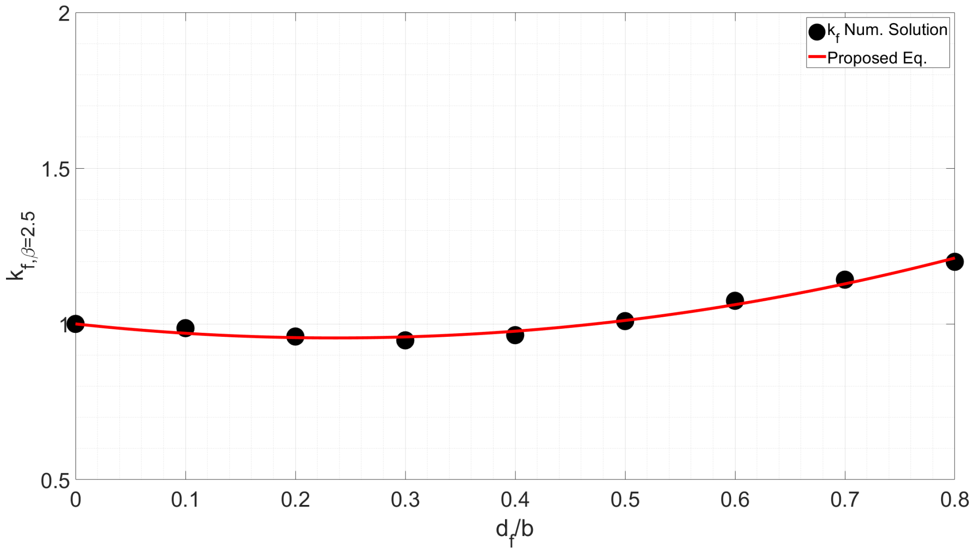

Figure 60: Fit equation of $k_{f,app.,\beta=2.5}$, with a determination factor $R^2 = 0.98320$

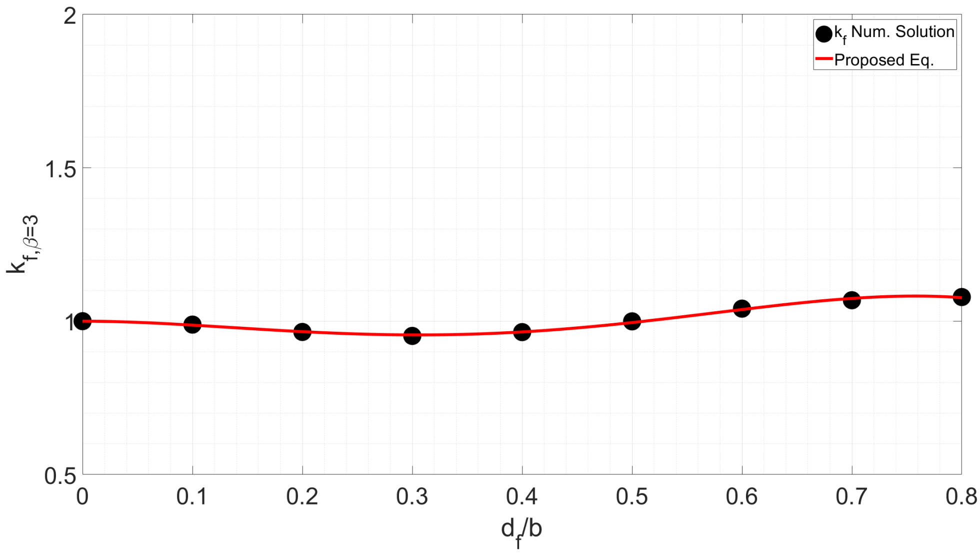

Figure 61: Fit equation of $k_{f,app.,\beta=3}$, with a determination factor $R^2 = 0.99545$

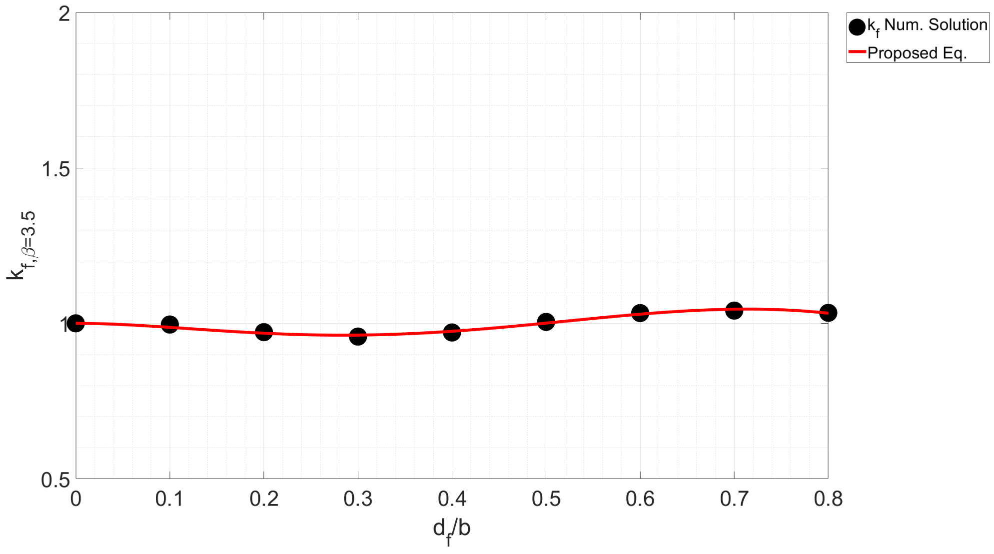

Figure 62: Fit equation of $k_{f,app.,\beta=3.5}$, with a determination factor $R^2 = 0.97526$

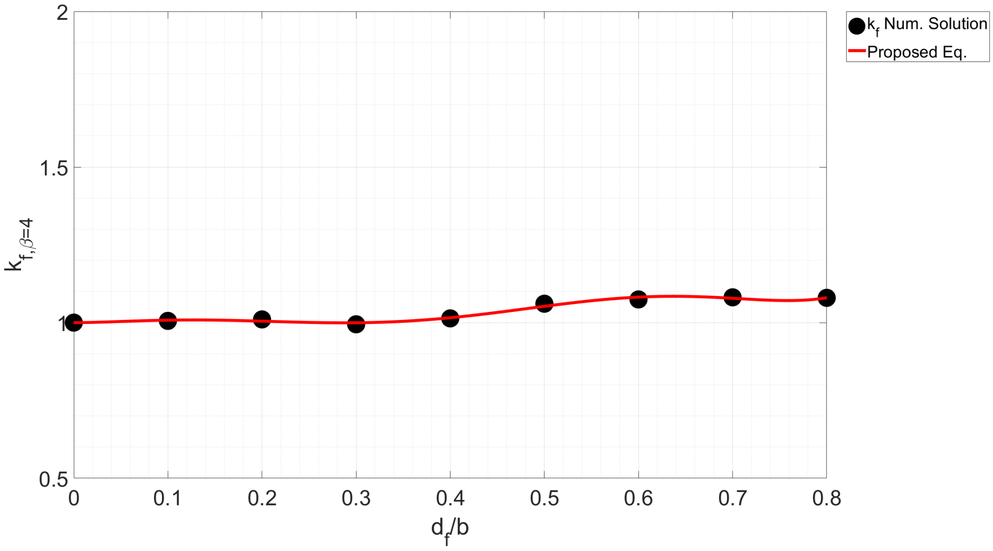

Figure 63: Fit equation of $k_{f,app.,\beta=0.5}$, with a determination factor $R^2 = 0.98208$

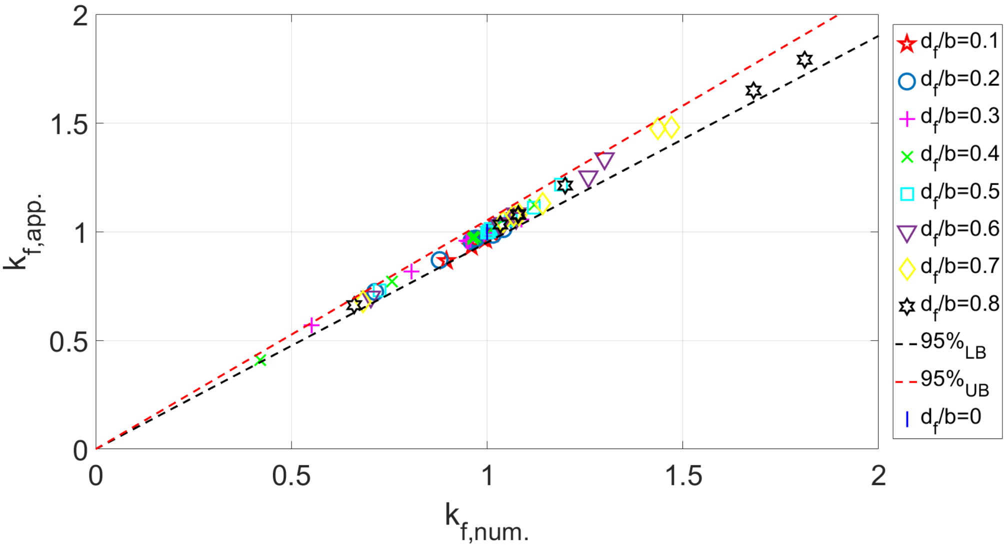

Figure 64: Comparison of non dimensional buckling coefficients (k_f) provided by Equation 81 and numerical solution within a confidence range of 95%.

Clearly, from Figure 64, all the solutions lie within an acceptable 95% confidence range, representing a good approximation from the proposed equation with the numerical solution.

To be able to provide a full closed form expression for the aspect ratio and hole diameter ratios, using the later equations, a function with these two variables are created. This approximation, is made as the first one, where the independent term is unitary, and all the factors that have almost no contribution are discarded. Also, the values of $\beta = 0.5$ are not considered, since this is an uncommon and unusual aspect ratio used (Figure 65). All the coefficients to build the equation are provided in Table 11.

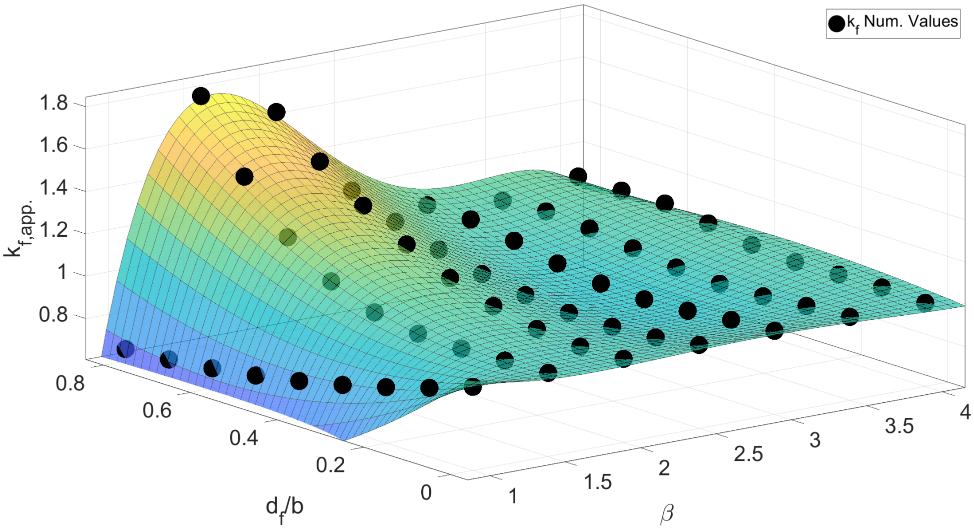

Figure 65: Fit surface of $k_{f,app.}$, with a determination factor of $R^2 = 0.94544$.

$$k_{f,app.}(\beta, \frac{d_f}{b}) = \sum_{i=0} \sum_{j=0} \alpha_{ij} \beta^i (\frac{d_f}{b})^j \tag{82}$$

Table 11: Coefficients α_{ij}.

α_{00}	α_{01}	α_{02}
1	-11.6209	0.8428
α_{10}	α_{11}	α_{12}
0	19.2838	0.2546
α_{20}	α_{21}	α_{22}
0	-11.3607	0
α_{30}	α_{31}	α_{32}
0	2.7676	-0.03060
α_{40}	α_{41}	α_{42}
0	-0.2372	0

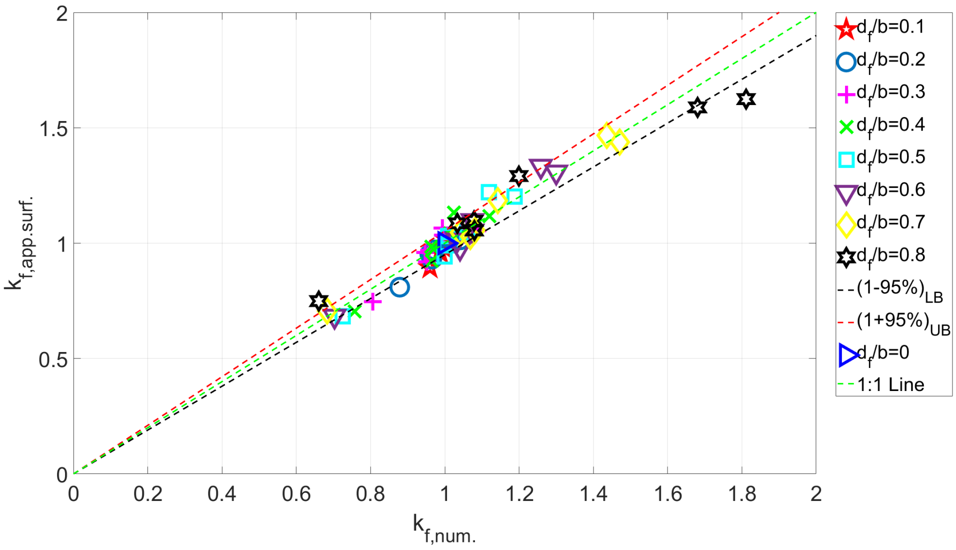

Figure 66: Comparison of non dimensional buckling coefficients (k_f) provided by Equation 82 and numerical solution within a confidence range of 95%.

Since the surface determination factor stayed below 95% (Figure 66), there are some solutions that may not be representative of the numerical solution. This general equation, should be used only for values of β, that are not covered by Equation 81.

To validate the accuracy of these equations, geometrically and materially non linear imperfection analyses were carried and compared against the experimental results. To model the imperfection, the shape factor (SF) parameter is given as:

$$SF = w_0 * \frac{1}{d_{l,num.}} \tag{83}$$

where, $d_{l,num.}$, is the maximum lateral displacement given by the *Eigenvalue* buckling analysis, and w_0 is the imperfection value.

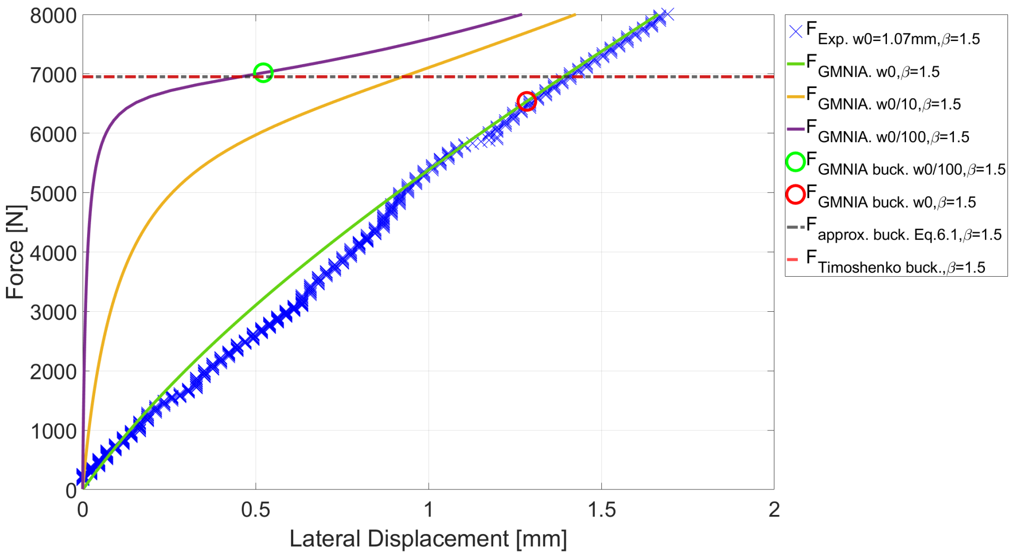

Figure 67: Force vs lateral displacement for $\beta = 1.5$, using Eq 81.

Three shape factors are analyzed: $w_0 = w_{0,real}$; $w_0 = w_0/10$; $w_0 = w_0/100$. Figure 68, can clearly visually provide the trend, when the shape factor is decreasing, revealing the critical buckling load from the experimental model tested (since is has a large value of imperfection). The critical load was found by evaluating the first large difference in lateral displacement.

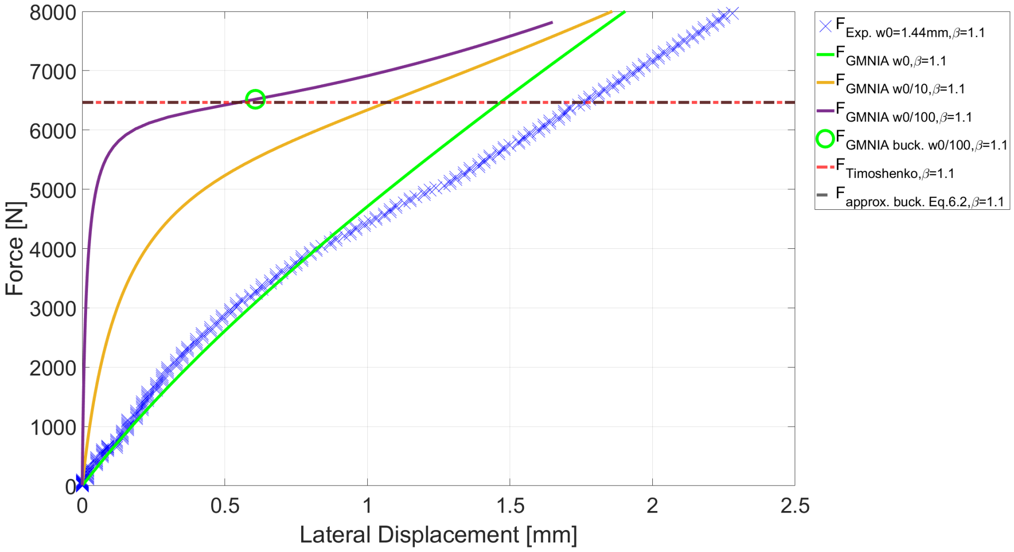

Figure 68: Force vs lateral displacement for $\beta = 1.1$, using Eq. 82.

7 Conclusions

From the discussion presented earlier, the following conclusions and recommendations can be made:

- The analytical solution presented in this study, for a plate under compression with all borders simply supported, can't be used to predict the buckling load of plates with central cut-outs with d_f/b ratios over 0.1, since it produces unrealistic values (only supports global buckling modes).
- The best overall configuration, which holds the most buckling load, are the aspect ratios of $\beta = 2$ and $\beta = 4$, with a d_f/b ratio of 0.5. These configurations provide the high buckling mode during the analysis.
- Square plates and rectangular plates cannot be compared, and have totally different buckling behavior. The shifting in buckling mode when the d_f/b ratio is increasing, can place the central hole in a bad position (line of maximum amplitude of the sinusoidal wave buckling shape).
- For odd values of β, the buckling mode m is always equal to the aspect ratio, independently of the d_f/b ratio.
- Proposed equation could predict the buckling load of the experimental procedures, with a relative error of 0.82% for $\beta = 1.1$ and 0.96% for $\beta = 1.5$, validating its accuracy.
- Proposed equations align with the numerical results, which means, that can be effectively used to predict the buckling load of compressed plates with simply supported edges, with central cutouts, in the analyzed range.

8 Future Work

While this dissertation has contributed to the understanding of the interaction of circular cut outs in simply supported plates under compression, in the elastic regime, other relevant aspects remain open for further investigation.

The analytical model developed was restricted to plates with central circular openings with simply supported borders, and to get an explicit value of k_g, simplifications were made to transform the circular boundary condition into a square. Numerical simulations assumed ideal boundary conditions and initial geometrical imperfections, while experimental procedures were limited to solid plates without openings. Also, the formulation should be extended to cover other non circular perforation geometries, different or partially restrained boundary conditions to replicate the flange stiffness.

Over numerical development, the model can incorporate initial imperfections and residual stresses to better replicate the realistic behavior, as including strain hardening and fracture. Other parametric studies should be evaluated, such as, number and spacing of perforations, and web hole positioning.

Further experimental work is needed, since it was limited to solid plates without any perforation. Tests on perforated plates, with varying aspect ratios and d_f/b ratios, should be made, along with proper instrumentation positioning. Different boundary conditions for the plates should be tested, as for different slenderness values, evaluating the transition from plastic yield of the cross section to failure by elastic buckling behavior.

By attending these guidelines, future research can provide more comprehensive design guidance for cellular steel beams, by linking theoretical formulations, numerical simulations, and real world performance, while providing safer, efficient and sustainable applications.

References

American Society of Civil Engineers. (1999). *Specification for structural steel beams with web openings* (SEI/ASCE 23-97) [ASCE Standard]. https://ascelibrary.org/

ANSYS. (2024). SHELL181 [[Online; accessed 04-May-2024]].

Bazant, Z. P., & Cedolin, L. (2010). *Stability of structures: Elastic, inelastic, fracture and damage theories* (1st). World Scientific Publishing Company.

Braga, J. J., Linhares, D. A., Cardoso, D. C., & Sotelino, E. D. (2021). Failure mode and strength prediction of laterally braced litzka-type castellated beams. *Journal of Constructional Steel Research*, *184*. https://doi.org/10.1016/j.jcsr.2021.106796

Brown, C. J., Yettram, A. L., & Burnett, M. (1987). Stability of plates with rectangular holes. *Journal of Structural Engineering*, *113*(5), 1111–1116. https://doi.org/10.1061/(ASCE)0733-9445(1987)113:5(1111)

CEN/TC 250/SC 3. (2005). *Eurocode 3: Design of steel structures – part 1-1: General rules and rules for buildings*. European Committee for Standardization.

CEN/TC 250/SC 3. (2017, December 14). *Eurocode 3 - design of steel structures - part 1-13: Steel beams with large web openings* (Working Draft No. CEN/TC 250/SC 3 N 2529) (Prepared by WG 20 of SC3 and PT 2 of SC4). European Committee for Standardization.

Chen, X. W., Yuan, H. X., Du, X. X., Zhao, Y., Ye, J., & Yang, L. (2018). Shear buckling behaviour of welded stainless steel plate girders with transverse stiffeners. *Thin-Walled Structures*, *122*, 529–544. https://doi.org/10.1016/j.tws.2017.10.043

Chung, K. F., Liu, T. C. H., & Ko, A. C. H. (2001). Investigation on vierendeel mechanism in steel beams with circular web openings. www.elsevier.com/locate/jcsr

Darwin, D. (1990). *Steel design guide series: Steel and composite beams with web openings* (Second Printing: September 1991, Third Printing: October 2003) [Copyright © 1990 by American Institute of Steel Construction, Inc. All rights reserved.]. American Institute of Steel Construction, Inc.

El-Sawy, K. M., & Nazmy, A. S. (2001). Effect of aspect ratio on the elastic buckling of uniaxially loaded plates with eccentric holes. *Thin-Walled Structures*, *39*(12), 983–998. https://doi.org/10.1016/S0263-8231(01)00040-4

European Committee for Standardization. (2005, May). *Eurocode 3: Design of steel structures – part 1-1: General rules and rules for buildings* [Supersedes ENV 1993-1-1:1992; Incorporating Corrigenda February 2006 and March 2009]. CEN (European Committee for Standardization).

European Committee for Standardization. (2006, October). *Eurocode 3: Design of steel structures – part 1-5: Plated structural elements* [Supersedes ENV 1993-1-5:1997; Incorporating corrigendum April 2009]. CEN.

França, G. M., Weidlich, C. M., Sotelino, E. D., & Cardoso, D. C. (2022). An appraisal of the vierendeel mechanism capacity of cellular beams with sinusoidal openings. *Journal of Constructional Steel Research*, *198*. https://doi.org/10.1016/j.jcsr.2022.107539

Hingnekar, D. R., & Vyavahare, A. Y. (2023). Shear resistance of steel plate girder end panels. *Iranian Journal of Science and Technology - Transactions of Civil Engineering*, *47*, 2311–2332. https://doi.org/10.1007/s40996-023-01064-3

Institution, B. S. (1990, February). *Structural use of steelwork in building - part 1: Code of practice for design in simple and continuous construction: Hot rolled sections* [Incorporates Amendment No. 1 (AMD 6972, February 1992)]. British Standards Institution (BSI). https://www.bsigroup.com/

Jia, L. G., Bi, R., Lang, Y. X., & Li, X. F. (2020). Experimental study and theoretical analysis on seismic performance of castellated beam with hexagonal holes. *Advanced Steel Construction*, *16*, 233–246. https://doi.org/10.18057/IJASC.2020.16.3.5

Jia, L., Li, Q., Ji, W., Chen, C., Du, J., & Geng, K. (2024). Influence of the local buckling of web on the bearing capacity of a castellated beam/composite beam under pure bending. *Structures*, *63*, 106358. https://doi.org/10.1016/j.istruc.2024.106358

Kang, L., Hong, S., & Liu, X. (2021). Shear behaviour and strength design of cellular beams with circular or elongated openings. *Thin-Walled Structures*, *160*, 107353. https://doi.org/10.1016/j.tws.2020.107353

Komur, M. A., & Sonmez, M. (2008). Elastic buckling of rectangular plates under linearly varying in-plane normal load with a circular cutout. *Mechanics Research Communications*, *35*(4), 361–371. https://doi.org/10.1016/j.mechrescom.2008.01.005

Kumai, T. (1952). Elastic stability of the square plate with a central circular hole under edge thrust. *Reports of Research Institute for Applied Mechanics*, *1*(2), 1–10. https://hdl.handle.net/2324/7153579

Lapira, L., Gardner, L., & Wadee, M. A. (2023). Elastic local buckling formulae for thin-walled i-sections subjected to shear and direct stresses. *Thin-Walled Structures*, *182*, 110150. https://doi.org/10.1016/j.tws.2022.110150

Lee, S. C., Lee, D. S., & Yoo, C. H. (2012). New shear design criteria for plate girders. *Proceedings of the Annual Stability Conference, Structural Stability Research Council*, 1–12. https://doi.org/10.1061/(ASCE)0733-9445

Mousa, E. A., El-Boghdadi, M. H., & Yossef, N. M. (2021). Flange yield and load/deflection in plate girders with different types of end stiffeners. *Structures*, *34*, 3915–3930. https://doi.org/10.1016/j.istruc.2021.10.016

Oribi, S. B., Kada, A., Lamri, B., & Mesquita, L. (2023). Behaviour of cellular steel beams at ambient and high-temperature conditions [Available online 6 May 2023. This is an open access article under the CC BY license.]. *Journal of Constructional Steel Research*, *207*, 107969. https://doi.org/10.1016/j.jcsr.2023.107969

Qiao, P., & Shan, L. (2005). Explicit local buckling analysis and design of fiber-reinforced plastic composite structural shapes. *Composite Structures*, *70*, 468–483. https://doi.org/10.1016/j.compstruct.2004.09.005

Reis, A., Lopes, N., Real, E., & Real, P. V. (2016). Numerical modelling of steel plate girders at normal and elevated temperatures. *Fire Safety Journal*, *86*, 1–15. https://doi.org/10.1016/j.firesaf.2016.08.005

Reis, A., Lopes, N., & Vila Real, P. (2019). Ultimate shear strength of steel plate girders at normal and fire conditions. *Thin-Walled Structures*, *137*, 318–330. https://doi.org/10.1016/j.tws.2019.01.013

Shanmugam, N. E., & Dhanalakshmi, M. (2001). State-of-art review and compilation of studies on perforated thin-walled structures. *International Journal of Structural Stability and Dynamics*, *1*, 59–81.

Standards Australia. (2020, August 21). *AS 4100:2020 Steel Structures* [ISBN 978 1 76072 947 9]. Standards Australia. https://www.standards.org.au

Sweedan, A. M., & El-Sawy, K. M. (2011). Elastic local buckling of perforated webs of steel cellular beam–column elements. *Journal of Constructional Steel Research*, *67*, 1115–1127. https://doi.org/10.1016/j.jcsr.2011.02.004

Szilard, R. (2004). *Theories and applications of plate analysis: Classical, numerical and engineering methods*. John Wiley & Sons.

Timoshenko, S., & Gere, J. M. (1989). *Theory of elastic stability* (2nd). Dover Publications.

Tsavdaridis, K. D., & D'Mello, C. (2011). Web buckling study of the behaviour and strength of perforated steel beams with different novel web opening shapes. *Journal of Constructional Steel Research*, *67*, 1605–1620. https://doi.org/10.1016/j.jcsr.2011.04.004

Wang, P., Ma, Q., & Wang, X. (2014). Investigation on vierendeel mechanism failure of castellated steel beams with fillet corner web openings. *Engineering Structures*, *74*, 44–51. https://doi.org/10.1016/j.engstruct.2014.05.008

Wang, P., Augustyn, K., Gomez, A., Quiel, S., & Garlock, M. (2019). Influence of boundary conditions on the shear post-buckling behavior of thin web plates. *Proceedings of the Annual Stability Conference, Structural Stability Research Council.*

White, D. W., & Barker, M. G. (2008). Shear resistance of transversely stiffened steel i-girders. *Journal of Structural Engineering*, *134*(9), 1425–1436. https://doi.org/10.1061/(ASCE)0733-9445(2008)134:9(1425)

Zhu, Z., Li, X., Chen, Q., & Cai, Y. (2022). Shear buckling of ship plates with different holes. *Mechanics & Industry*, *23*(4), Article 85. https://doi.org/10.1051/meca/2022004

Ziemian, R. D. (Ed.). (2010). *Guide to stability design criteria for metal structures* (6th). John Wiley & Sons, Inc.